Crystallographic snapshots of the Dunathan and quinonoid intermediates provide insights into the reaction mechanism of Group II decarboxylases

Subash Chellam Gayathri[1], Narayanan Manoj[1]*

[1] Department of Biotechnology, Bhupat and Jyoti Mehta School of Biosciences,
Indian Institute of Technology Madras, Chennai-600036, INDIA

* Corresponding Author, E-mail: nmanoj@iitm.ac.in

Journal of Molecular Biology, Volume 432, Issue 24, 2020, 166692,
https://doi.org/10.1016/j.jmb.2020.10.026.

ABSTRACT

PLP-dependent enzymes catalyze a plethora of chemical reactions affecting diverse physiological functions. Here we report the structural determinants of the reaction mechanism in a Group II PLP-dependent decarboxylase by assigning two early intermediates. The *in-crystallo* complexes of the PLP bound form, and the Dunathan and quinonoid intermediates, allowed direct observation of the active site interactions. The structures reveal that a subtle rearrangement of a conserved Arg residue in concert with a water-mediated interaction with the carboxylate of the Dunathan intermediate, appears to directly stabilize the alignment and facilitate the release of CO_2 to yield the quinonoid. Modeling indicates that the conformational change of a dynamic catalytic loop to a closed form controls a conserved network of hydrogen bond interactions between catalytic residues to protonate the quinonoid. Our results provide a structural framework to elucidate mechanistic roles of residues that govern reaction specificity and catalysis in PLP-dependent decarboxylation.

Keywords: Crystal structure; PLP-dependent decarboxylation; *In-crystallo* complexes, Reaction intermediates

ABBREVIATIONS: PLP, Pyridoxal 5′-phosphate; SB, Schiff base; N_{SB}, SB-nitrogen; QM/MM, quantum mechanics/molecular mechanics; AAT, aspartate aminotransferase; MjDC, Tyrosine decarboxylase from *Methanocaldococcus jannaschii*; LLP, internal aldimine; PLY, pre-decarboxylation intermediate; QND, quinonoid-like intermediate; PSB, protonated N_{SB}; DDC, DOPA decarboxylase; HDC, histidine decarboxylase; TyDC, tyrosine decarboxylase; TPL, tyrosine phenol lyase; DGD, dialkylglycine decarboxylase; L-Tyr, L-tyrosine; CL, catalytic loop.

INTRODUCTION

The catalytic versatility of pyridoxal 5'-phosphate (PLP) arises from its ability to form Schiff base (SB) aldimines with substrates and stabilize subsequent carbanionic intermediates *via* its electrophilic pyridine system. Formation of the external aldimine intermediate with the substrate, commonly an α-amino acid, is a common step in all PLP-dependent reactions (Scheme S1). This promotes the heterolytic cleavage of one of the other three bonds associated with the substrate carbon atom that is attached to the SB nitrogen. Deprotonation or decarboxylation from the carbon atom resulting in the carbanionic quinonoid intermediate initiates a majority of the diverse PLP-catalyzed reactions that include transamination, α/β elimination, racemization, retro-aldol cleavage and decarboxylation. In PLP-dependent enzymes, control of the reaction type, the substrate specificity, and the kinetic properties, is enforced by the active site environment [1,2,3,4,5,6]. Reaction specificity is primarily dictated by stereoelectronic effects that maximize resonance stabilization of the forming carbanion by orienting the leaving group bond geometry in the "Dunathan-alignment", i.e., orthogonal to the conjugated π-system of the cofactor (Scheme 1) [1,2]. Dunathan originally proposed that PLP-dependent enzymes are evolved to specifically bind and optimally orient the external aldimine intermediate in this alignment to achieve the transition state.

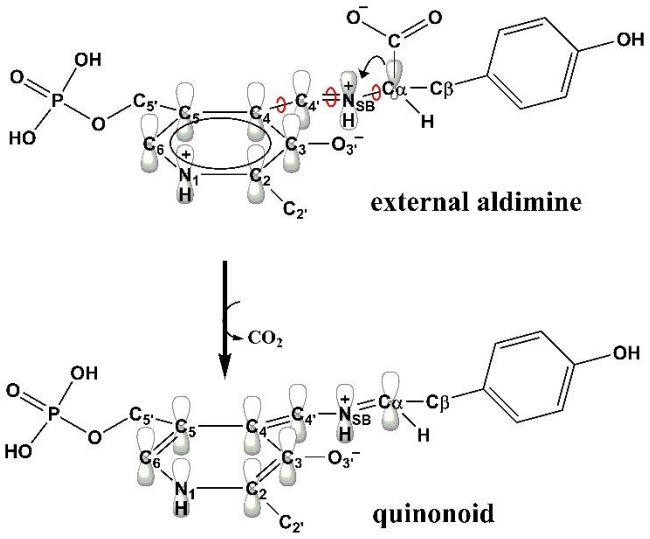

Scheme 1. Decarboxylation reaction catalyzed by PLP-dependent decarboxylases. The three torsion angles that affect the geometry of the Dunathan and quinonoid intermediates are shown as red arcs.

Catalytic effects in these enzymes can be augmented by electronic modulation, wherein protonation profiles of the four ionizable groups in PLP (pyridine-nitrogen (N1), SB-nitrogen (N_{SB}),

phenolic-oxygen (O3') and phosphate group), influenced by the active site micro-environment, destabilizes the ground-state to affect reaction rate and specificity [6,7]. However, recent quantum mechanics/molecular mechanics (QM/MM) work with docked substrates in aspartate aminotransferase (AAT) demonstrated that a σ→π* hyperconjugation interaction between the Cα-bonding to N_{SB}-C4′ antibonding orbital occurring in the Dunathan-alignment stabilizes the ground state and instead enhances rate by strongly favoring the Dunathan intermediate [8]. The exact mechanism by which catalytic competence of PLP-dependent enzymes is achieved is still a matter of debate and is enzyme-dependent [8,9,10,11]. For instance, in an unusual case, dialkylglycine decarboxylase (DGD) displays both aminotransferase and decarboxylase activities for amino acid substrates and the reaction specificity depends on the size of the substrate side chain. Exhaustive kinetic studies using active site residue variants led to the postulate that the substrate side chain size induces different modes of Dunathan-alignment for each substrate, and unique, subtle interactions with active site residues control the preference of one reaction over the other [4,6,12,13].

Current mechanistic insights from the two reaction intermediates that are common to all PLP-dependent enzymes, namely, the external aldimine and quinonoid states, are primarily derived from enzymes that perform heterolysis at the Cα–H σ bond and comes with a potential caveat. At the reported resolutions, it is challenging to visualize H atoms using X-ray crystallography, and the external aldimine (Cα–H) is almost indiscernible from the quinonoid (Cα) [14,15,16]. Consequently, the structural determinants of the required geometry of interactions for reaction specificity and conformational changes associated with successive steps in the catalytic cycle beyond external aldimine formation, remain less well understood. In contrast, decarboxylases are particularly useful in inspecting the structural enzymology of all PLP-dependent enzymes since the heterolytic Cα–C bond can be observed. However, it has generally been challenging to obtain relevant structural snapshots in these enzymes since the reaction intermediates of decarboxylation are short-lived. It is intriguing that the complete cognate Dunathan-alignment has not been directly captured in the structure of a PLP-dependent decarboxylase, to date (Table S1). Furthermore, the indispensable quinonoid intermediate is unstable due to facile protonation by catalytic residues, preventing its analysis by crystallographic methods, leaving many structural details uncharacterized. Structural data from these complexes are crucial to understanding how the geometry of active site interactions optimize the stereoelectronic and protonation states, and how the desired reaction outcome from the quinonoid intermediate is controlled while limiting other likely reactions.

Previously, we reported the biochemical characterization and the crystal structure of an archaeal tyrosine decarboxylase from *Methanocaldococcus jannaschii* (MjDC) in the internal-aldimine state with the SB residue Lys245 (holoMjDC•LLP, PDB ID: 6JY1). MjDC is a homodimeric Group II PLP-dependent decarboxylase belonging to the fold type-I transferase superfamily and displays the characteristic three-domain architecture of the fold. Comparative analysis of this form with the PLP aldehyde bound form (apoMjDC•PLP_{ALD}, non-covalently bound, PDB ID: 3F9T) provided structural insights into the mechanism of internal aldimine formation [17,18]. In the present study, X-ray data from crystals of the K245A variant soaked with PLP and L-Tyr, allowed the *in-crystallo* capture of the pyridoxal-P bound form, the external aldimine form in the Dunathan-alignment, and the quinonoid bound form. Along with activity assays of catalytic site residue variants, the high-resolution snapshots of these successive reaction intermediates have revealed key structural determinants and associated conformational changes required for the catalytic cycle of the decarboxylase.

RESULTS AND DISCUSSION

K245A variant shows external aldimine formation with substrate L-Tyr in solution

Consistent with the transient nature of the external aldimine and quinonoid intermediates, our efforts to capture these complexes with the wild type (WT) enzyme proved unsuccessful. Therefore, we employed the SB residue mutant (K245A in MjDC) to serve as a relevant model for the description of the mechanism of decarboxylation, based on kinetic data from the close homolog, L-DOPA decarboxylase (DDC). In DDC, an alanine mutant of the SB lysine decreased the rate of decarboxylation by 1500-fold while not significantly affecting the formation of the product external aldimine. Rather, the variant largely impaired affinity for PLP and product amine release [19,20]. To establish the competence of the MjDC K245A variant to form the external aldimine with the cognate substrate (L-Tyr), the following experiments were carried out.

The WT and the K245A mutant proteins were purified to homogeneity, and the dimeric forms were confirmed (Figure 1a). The WT displays the highest activity at 90 °C, pH 8.0 in an endpoint assay that only detects for the released amine product of decarboxylation of L-Tyr, i.e., tyramine [18]. The activity of the K245A variant could not be detected in the endpoint assay, as was expected (Figure 1b) [19,20]. Therefore, reaction progress was monitored using UV-vis absorbance spectra to confirm whether the mutant was suitable to study the decarboxylation step. Initially, WT spectra were taken at 70 ºC to confirm reaction progress. Next, spectral scans were taken at lower temperatures (30 or 24 ºC) to slow down the reaction and detect the intermediates,

since the WT shows a 40% lowering of specific activity [18]. The WT showed absorption maxima at 414 nm at 30 ºC and 420 nm at 70 ºC, corresponding to the presence of the internal aldimine. Upon addition of L-Tyr, an immediate red shift was observed in the absorbance maxima from 414 to 421 nm (30 ºC) and from 420 nm to 423 nm (70 ºC) (Figure 1c, d, red line), indicating reaction progress and formation of the external aldimine at both temperatures (Figure 1c, d).

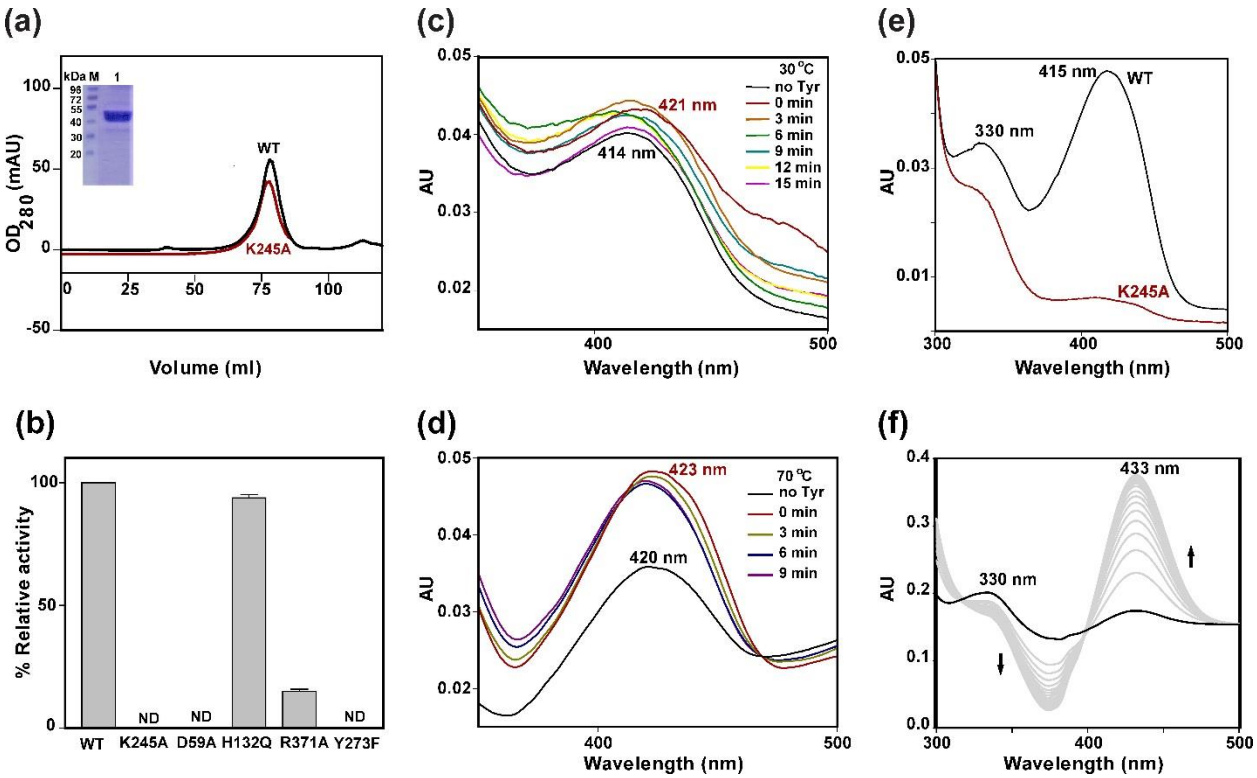

Figure 1. Characterization of K245A MjDC (a) Size exclusion elution profile of the WT (black line) and the K245A variant (red line) confirming dimeric forms. Inset shows the SDS-PAGE profile of purified K245A. (Lane M: Protein ladder, Lane 1: K245A ~45 kDa) (b) Comparison of decarboxylation activity of MjDC and variants. The specific activity of the WT enzyme towards L-Tyr was measured using an endpoint assay as described in the Experimental Procedures and is set to 100 %. K245A, D59A and Y273F mutants show no detectable (ND) activity under standard assay conditions [18]. The error bar represents the standard deviation between triplicates. (c), (d) Time course of UV-visible absorption spectra of the WT with substrate L-Tyr measured at 30 ºC and 70 ºC. Black lines correspond to the spectrum before the addition of the substrate. The colored lines correspond to successive spectral scans recorded at 3 min intervals upon addition of the substrate. Two shoulder peaks at ~490 nm (red line) and 410 nm (green line) apart from the aldimine peaks (414/421 nm) were observed at 30 ºC whereas only the aldimine peaks (420/423 nm) were observed at 70 ºC. (e) UV-visible absorbance spectra of recombinant WT and K245A at 24 °C. Spectral scans show evidence for decreased PLP content in purified K245A in the absence of externally added PLP, in comparison to the WT. Absorbance maxima in the WT (~320 nm and 415 nm) correspond to the tautomers of the internal-aldimine. The absorption spectra of K245A show an altered spectrum with broad bands centred at ~320 nm and ~405 nm, consistent with absence of the internal aldimine. (f) UV-visible difference spectra of K245A with L-Tyr and PLP shows maxima at ~330 nm and ~433 nm (solid black line). The light grey lines correspond to successive spectral scans recorded every 30 s after incubation with substrate for 5 min. The dark grey line corresponds to a spectral scan taken after 15 min of incubation.

Next, we tested the activity and spectroscopic properties of the K245A variant. The spectra of K245A shows evidence for decreased PLP binding, as expected (Figure 1e) [20]. However, when incubated with L-Tyr and PLP at room temperature (RT), the K245A difference spectra showed absorption maxima at ~330 nm and ~433 nm (Figure 1f, solid black line when measured immediately upon addition of K245A after blanking with PLP and L-Tyr). The 433 nm peak conceivably corresponds to the external aldimine in K245A and is consistent with the spectral change of the SB mutant of DDC with L-DOPA [20]. With an increase in time, the spectra show an increase in absorbance at 433 nm, possibly due to an accumulation of this intermediate (Figure 1f). In the WT, the spectral changes were more prominent at 30 ºC during reaction progress and two shoulder peaks at 410 nm (Figure 1c, green line) and 490 nm (Figure 1c, red line) were observed in addition to the aldimine peaks. However, the exact peak (~500 nm) corresponding to the quinonoid intermediate could not be observed in the solution spectra of both the WT and K245A. Nevertheless, prior literature indicates that detecting quinonoid formation in decarboxylases with true substrates is not trivial due to the rapid protonation of the quinonoid, although it is well established that the quinonoid is an intermediate of the decarboxylation reaction [2,4,9,10,11,20,21,22,].

Structure of the Pyridoxal-P bound form (PLP-K245A)

Having established the competence of the K245A in the formation and binding of the external aldimine with L-Tyr in solution, we used this variant for extensive crystallization trials to capture different active site states of the enzyme. Crystal structures of four different states of K245A were determined, and include the cofactor-free apo-K245A form, the PLP-K245A form (PLP aldehyde complex), the PLY-K245A form (external aldimine complex) and the QND-K245A form (quinonoid complex). All four crystals were isomorphous with each other and contained one subunit in the asymmetric unit. The crystallographic data are summarized in Table 1. The structures display the characteristic architecture of the fold-type I superfamily, and as previously described, comprises of three domains, an N-terminal domain (residues 1-30), a PLP-binding large domain (residues 30-302) and a small C-terminal domain (residues 303-395) [23]. Residues (269/270–278) of the catalytic loop (CL), and residues 364–366 of a C-terminal loop were disordered and not modelled in all the structures (Figure 2a). The pairwise root mean square deviation (rmsd) of the Cα atoms between these variants and that of the WT apo and holo forms (apoMjDC•PLP_{ALD}, holoMjDC•LLP) are less than 0.5 Å, indicating that the overall conformation of MjDC is not affected either by the mutation or the bound ligands in the active site (Figure 2b and Table S2). The functional

homodimer is formed by two subunits related by a crystallographic 2-fold axis and identical to that observed in homologs. The two active-sites are formed at the inter-subunit interface of the dimer (Figure 2c, d) [24,25,26].

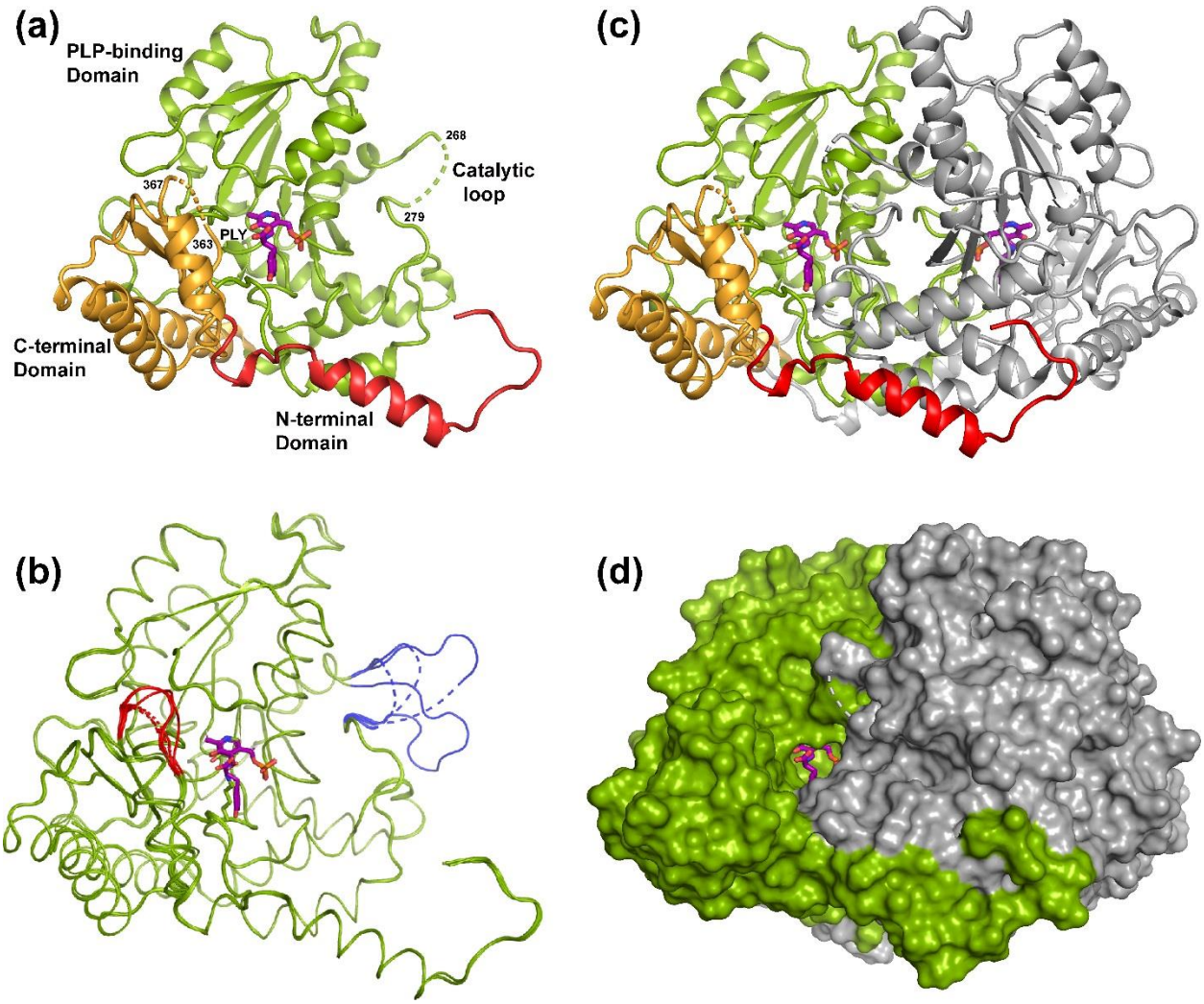

Figure 2. Structure of PLP-K245A and comparison of structures (a) Ribbon representation of a single subunit of K245A showing its overall fold. The three domains are highlighted in different colors (PLP binding domain in green, C-terminal domain in orange and N-terminal domain in red, PLY is shown as purple sticks). Dashes between residues 268–279 (catalytic loop, CL) and 363–367 (C-terminal loop, CTL) indicate missing segments. (b) Superposition of apoMjDC•PLP_{ALD} (PDB ID: 3F9T), holoMjDC•LLP (PDB ID: 6JY1) and the three K245A complexes is shown in Cα trace representation. The ligands are shown as purple sticks. The CL and the CTL are highlighted in blue and red, respectively. Note that the CL is completely ordered only in apoMjDC•PLP_{ALD} (blue solid line) whereas it is disordered (blue dashed lines) in holoMjDC•LLP and in all K245A complexes. The CTL in the K245A structures is also disordered (red dashed lines)[18]. (c) Ribbon diagram showing the dimeric form of the PLY-K245A structure. The three domains of one subunit are colored as in panel (a) and the second subunit is shown in grey. The CL of the second subunit is shown as black dashed lines. (d) Surface representation of the PLY-K245A dimer showing the open active site pocket of one subunit at the dimer interface. The two subunits are colored green and grey. The CL region of the *trans* subunit is shown in black and PLY is shown as purple sticks.

In the apo-K245A structure determined to 1.81 Å resolution, PLP had poor occupancy in the active site, consistent with the spectroscopic data (Figure 1e). Pyridine part of the cofactor could not be modelled, although phosphate had full occupancy (Figure S1). As a result, several residues and some water molecules at the inter-subunit interface also appear affected. Hence the structure was not investigated further and is not presented. To improve the occupancy of the bound ligand, the apo-K245A crystals were soaked with excess PLP, and diffraction data collected on these crystals. The soaking experiment did not affect the unit cell parameters or the dimeric arrangement. The structure of PLP-K245A at 1.79 Å, clearly confirmed the presence of PLP in the active site (Figure 3b, Figure S2). PLP in the aldehyde form (Pyridoxal-P) was modelled in two conformations, and the geometry of interactions of one of the conformers is almost identical to those observed in the active site of apoMjDC•PLP_{ALD} (PDB ID: 3F9T), except here, a water molecule substitutes for the interactions made by the Nζ atom of Lys245 (Figure S3). Interestingly, in the alternate conformation of pyridoxal-P, the O4′-C4′-C4-C3 angle is 10º with the O4′ oriented towards the O3′ (2.6 Å) (Figure S3, inset). This geometry of pyridoxal-P corresponds to the proposed activated state of PLP in our previous study, where the extended delocalized π system activates the C4′ atom for nucleophilic attack by the substrate primary amine [18]. Finally, as a consequence of the dual conformations, several active site residues such as Phe133, Glu136, Arg371 and Glu182 assume dual conformations in PLP-K245A, consistent with the proposed coupling of the active site landscape with the PLP state (Figure S3) [18]. Thus, the structure of PLP-K245A proved to be a useful reference model for the identification and comparison of conformational changes associated with the PLY-K245A and QND-K245A reaction intermediate complexes (Figure 3).

Structure of the Dunathan intermediate complex (PLY-K245A)

Next, we used the PLP-K245A crystals to capture the external aldimine pre-decarboxylation intermediate (Dunathan intermediate) by soaking with L-Tyr. X-ray data collected at the synchrotron source after immediate flash freezing of PLP-K245A crystals soaked with L-Tyr for 10 s proved successful. The structure, refined to a resolution of 1.8 Å, displayed unambiguous electron density for the external aldimine complex with Tyr (PLY-K245A) with full occupancy. The maps clearly show *in-crystallo* SB formation between PLP and the primary amine of L-Tyr (Figure 3c, Figure S4). The phenolic ring of PLY is oriented towards the solvent accessible region of the active-site cavity. The substrate hydroxyl is stabilized by a hydrogen bond with Asp59′ (Oδ2) and a water-bridge interaction with the OH of Tyr28. The OT2 atom of the substrate-carboxylate is

solvent-exposed and is hydrogen-bonded to a water molecule and a conserved His132 (Nε2) residue. Similar interactions with the equivalent His residue were observed in the structures of human histidine decarboxylase (HDC) and pig DDC, with their respective inhibitors, histidine methyl ester, (PDB ID: 4E1O) and CarbiDOPA (PDB ID: 1JS3) [25,27]. Moreover, in a computational study using a docked tyrosine external aldimine in the active site of *Lactobacillus brevis* tyrosine decarboxylase (TyDC), the equivalent His residue was proposed to play an irreplaceable role in conformation stability of PLP and the substrate-carboxylate [10]. His132 is also a key residue participating in a conserved extended hydrogen-bonding network that was implicated in catalysis in our previous study (Figure 7a) [18]. Notably, the OT1 atom of PLY forms a water-mediated interaction (W_C) with a conserved Arg371 (Nη2) residue. The water-mediated interaction with the Arg371 and the OT1 atom of the aldimine has so far not been observed in any ligand-bound structures of Group II decarboxylases probably because these ligands do not represent the true geometry of an activated cognate external aldimine complex. (Table S1). For instance, in HDC, DDC, and a plant TyDC (PDB ID: 6EEM, chain B) the carboxylates of the ligands are farther away from the arginine (Arg447 in DDC and HDC; 482 in TyDC), or the ligand is not covalently attached to PLP (PDB ID: 6EEM, chain A; 6EEW) [25,27,28]. Furthermore, no other stabilizing or destabilizing interactions with the substrate carboxylate was observed in PLY-K245A. The active site interactions identified in this complex are also consistent with the observation of loss of activity of the D59A, R371A, and H132A mutants of MjDC (Figure 1b).

Structure of the quinonoid intermediate complex (QND-K245A)

Most interestingly, when we processed X-ray data collected at the home source (1.9 Å) from the PLY-K245A crystals soaked with L-Tyr for 48 h, we were surprised to find that the active site contained the post-decarboxylation quinonoid-like intermediate (QND-K245A). Unlike in the transaminases, in decarboxylases, a clear distinction can be made between the substrate-external aldimine and the quinonoid intermediate from the electron density maps (Scheme 1). Electron density corresponding to the carboxylate of L-Tyr is absent, whereas density consistent with a SB between the ligand and the cofactor can be observed (Figure 3d, Figure S5), indicating completion of the decarboxylation reaction *in-crystallo*. Furthermore, an additional peak (9.4 σ) in the difference map is present between the Nε2 atom of His132 and the Cα atom of QND. We first considered the possibility of radiation damage on the Cα-C bond of PLY, leading to the formation of the quinonoid-like state. The electron density geometry for this unknown ligand (UNL) appears trigonal planar and is inconsistent with a linear CO_2 molecule or a water molecule (Figure 4a). A

superposition of the omit maps of the PLY and QND intermediates reveals that the UNL electron density in the QND complex is discontinuous from that of the QND density (Figure 4a). The closest distance between the Cα and the UNL is 3.2 Å. Next, multiple data sets were collected using PLP-K245A crystals soaked with L-Tyr under different conditions such as different substrate concentrations, different soaking times, and different mounting intervals after freezing. Invariably in all data sets collected at the home source (data collection time ~ 6 hrs), the maps were indicative of the presence of QND and UNL, suggesting completion of the reaction at the end of data collection (For instance, Figure S6, represents one such dataset to 2.3 Å resolution, but is not reported here owing to poor occupancy of the ligand).

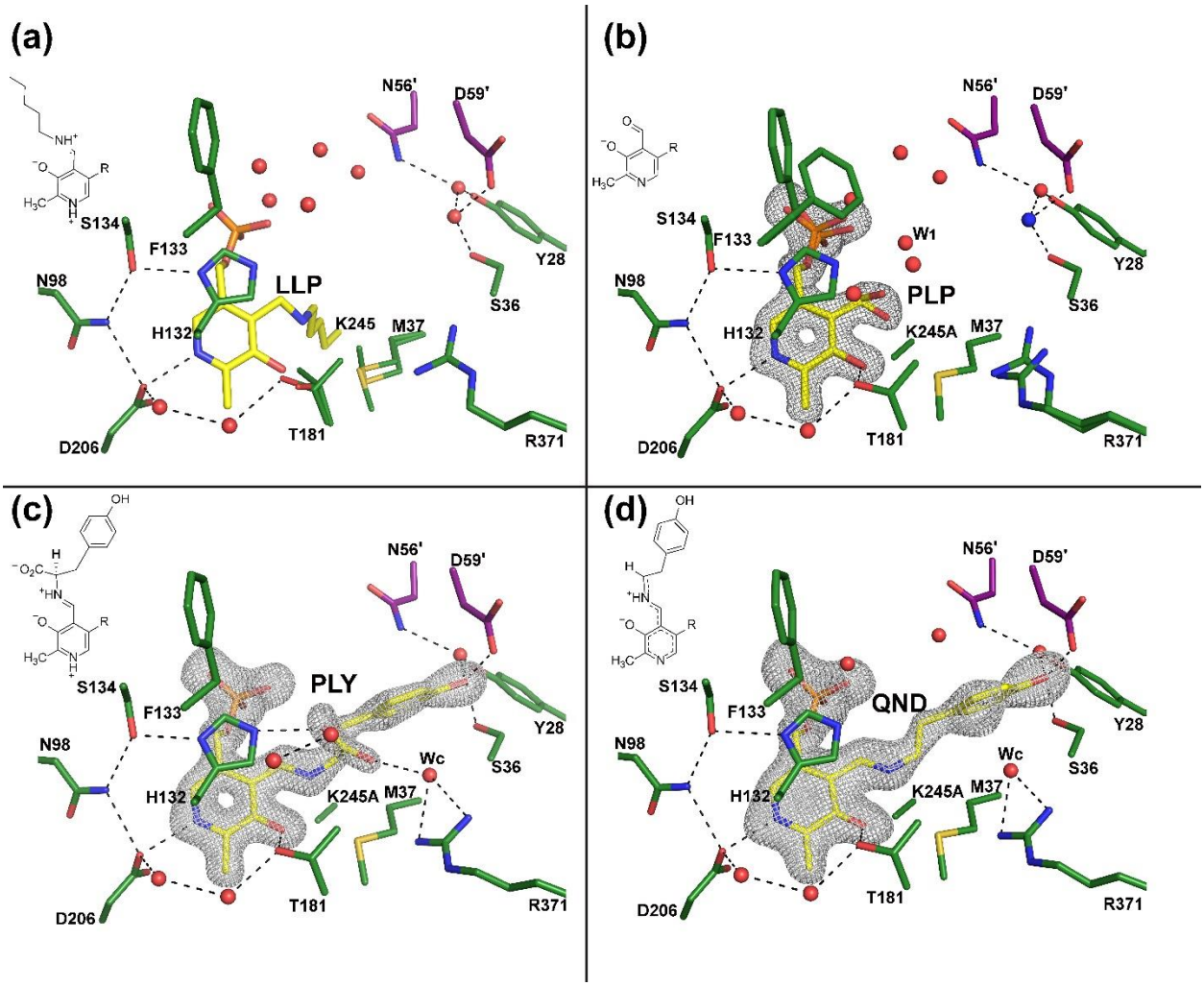

Figure 3. Reaction states during tyrosine decarboxylation in MjDC. Each panel shows a different intermediate (yellow sticks), proximate and extended-hydrogen-bonding network residues (green sticks) and waters (red spheres). Panel (a) shows the active-site of holoMjDC•LLP (PDB ID: 6JY1). Panels (b), (c) and (d) show the active-sites of K245A bound to pyridoxal-P (PLP), the pre-decarboxylation (PLY) and

post-decarboxylation (QND) intermediates, respectively. The structure of K245A bound to PLP was obtained only in the presence of excess added PLP. PLP was modelled in two alternate conformations in its active site as shown in panel (b). In the absence of external PLP, PLP was poorly bound in the acitve site of K245A (Figure S1). Ammonium ion is shown as blue sphere. Electron-densities in the corresponding mFo−DFc omit maps (contoured at 5.0 σ for PLP and PLY and 3.5 σ for QND) is shown as grey mesh. Neighboring subunit residues are colored purple. H-bonds are shown as black dashed lines.

It is noteworthy that we were able to obtain the pre-decarboxylation intermediate (PLY-K245A) only at the synchrotron source, and it appears that the shorter data collection time (~15 mins) facilitated the fortuitous capture of the PLY intermediate in the crystal. Moreover, there is no evidence for the bound UNL in the PLY complex. In contrast, the data for the post-decarboxylation intermediate containing the UNL were collected from crystals at the home source, where the likelihood of radiation damage is relatively lower (Table 1). To the best of our knowledge, there are no reported instances in literature for radiation damage resulting in decarboxylation of the Cα of Tyr or other amino acids that are bound as ligands in protein complexes.

To confirm the *in-crystallo* capture of these transient intermediates, we carried out spectroscopic, and mass spectrometry experiments on the substrate treated PLP-K245A crystals. Difference spectra using UV-visible spectroscopy collected from PLP-K245A crystals soaked with L-Tyr for ~3 hrs show three peaks at 410 nm, 430 nm, and 500 nm (Figure 4b, red line). The 430 nm peak corresponds to the expected external aldimine peak with the substrate in solution (Figure 1f). A prominent peak at ~500 nm corresponds to the expected absorption maxima from a quinonoid intermediate (Figure 4b, red line). The molecule responsible for the peak at 410 nm is unknown. However, a similar shoulder was also observed with the WT enzyme at 30 ºC, suggesting that this peak likely corresponds to a reaction intermediate (Figure 1c). In the spectral data collected from PLP-K245A crystals soaked with L-Tyr for 48 hrs, only the 500 nm peak corresponding to the quinonoid intermediate was observed and is in excellent agreement with the crystal structure (Figure 5a, black line). Thus, PLP-K245A crystals soaked with L-Tyr for ~3 hrs showed peaks indicative of the formation of both the PLY and QND intermediates. Furthermore, ESI-MS spectra collected from this crystal showed two unique peaks corresponding to the expected mass of both the PLY and QND intermediate compared to those collected from samples without the crystals and in good agreement with the spectroscopic data and the crystal structures (Figure 4c, d). The data unambiguously indicates that the PLY and QND states are indeed cognate intermediates of the decarboxylation reaction *in-crystallo* (Figure 5a), and that the QND intermediate is an outcome of a spontaneous decarboxylation reaction from PLY. Although the solution UV-visible spectra for the K245A did not indicate the formation of the quinonoid, we

believe that the reaction rate in the crystal was sufficiently slower to capture this usually elusive state unexpectedly. Thus, the K245A variant served as a competent model system that facilitated the capture of the first two consecutive steps of the decarboxylation pathway within a single active site.

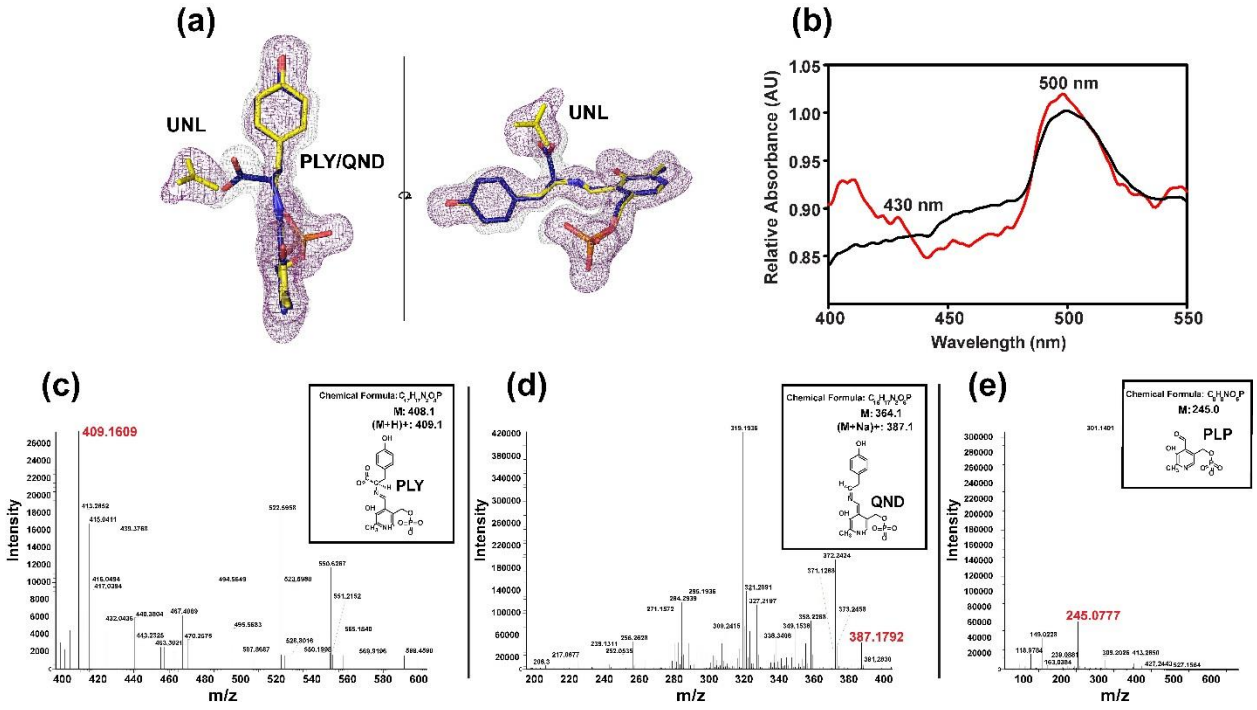

Figure 4. ***In-crystallo*** **characterization of the Dunathan intermediate and quinonoid complexes** (a) Two views (ca. ~270º) of the simulated annealing omit maps of Dunathan intermediate (PLY, grey mesh) and quinonoid (QND, purple mesh) contoured at 3σ, superposed on each other. The PLY (blue), QND (yellow) and UNL (yellow) ligands are shown as stick representation. (b) Difference absorbance spectra of PLP-K245A crystals soaked with L-Tyr. UV-visible difference spectra of PLP-K245A crystals were collected immediately (red line) and after 48 hrs (black line) upon soaking with L-Tyr. Peaks corresponding to the external aldimine (430 nm) and the quinonoid intermediate (500 nm) can be observed in the spectra collected from crystals for the shorter duration (red line). In the spectra collected after 48 hrs, only a single peak corresponding to the quinonoid intermediate can be observed. Panels (c), (d) and (e) show the ESI-MS spectra of PLP-K245A crystals soaked with L-Tyr. The peaks corresponding to the mass of PLY (c), QND (d) and PLP (blank) (e) are highlighted in bold solid line.

Decarboxylation is facilitated *via* hyperconjugation of the Dunathan intermediate

The geometry of the pre-decarboxylation intermediate here exemplifies all the requirements put forth by Dunathan for efficient catalysis [1,2]. In the PLY complex, the Cα atom is tetrahedral with sp^3-like hybridization with the C-Cα-N_{SB}-C4′ torsion angle ~87°, representing the Dunathan

alignment [2]. Remarkably, the Cα-N_{SB}-C4′-C4 and N_{SB}-C4′-C4-C3' angles are -161° and 1°, respectively (Scheme 1 and Figure 5b). This near coplanar conformation of PLY might facilitate hyperconjugation of the Cα σ-orbital with the π-orbital of the pyridine ring before decarboxylation, thereby weakening the Cα–C bond. Indeed, the observed geometry must be an accurate representation of the activated intermediate since it resulted in the capture of the next intermediate (QND-K245A) of the reaction with time, with no significant conformational change in the active-site residues (Figure 5a). The absence of large rearrangements during the catalytic cycle, from the internal aldimine state and further to the pre-decarboxylation and the post-decarboxylation states, is broadly in line with the expectation from computational studies that the molecular motions within the protein is minimum in these steps (Figure 3) [8,10]. In the QND, the Cα–C σ bond is lost, and the Cα acquires a trigonal planar geometry with *sp*^{2}-like configuration displaying an expected increase in coplanarity with the pyridine ring (Cα-N_{SB}-C4′-C4 = -179° and N_{SB}-C4′-C4-C3′ = 9°) (Figure 5c) [1,2,9]. These snapshots strongly indicate a transition of the reactants to a stable Dunathan-intermediate state *via* hyperconjugation as the driving force for the decarboxylation reaction, as opposed to a ground state destabilization or substrate distortion mechanism, and is in excellent agreement with recent QM/MM studies on AAT and LbTyDC [8,10].

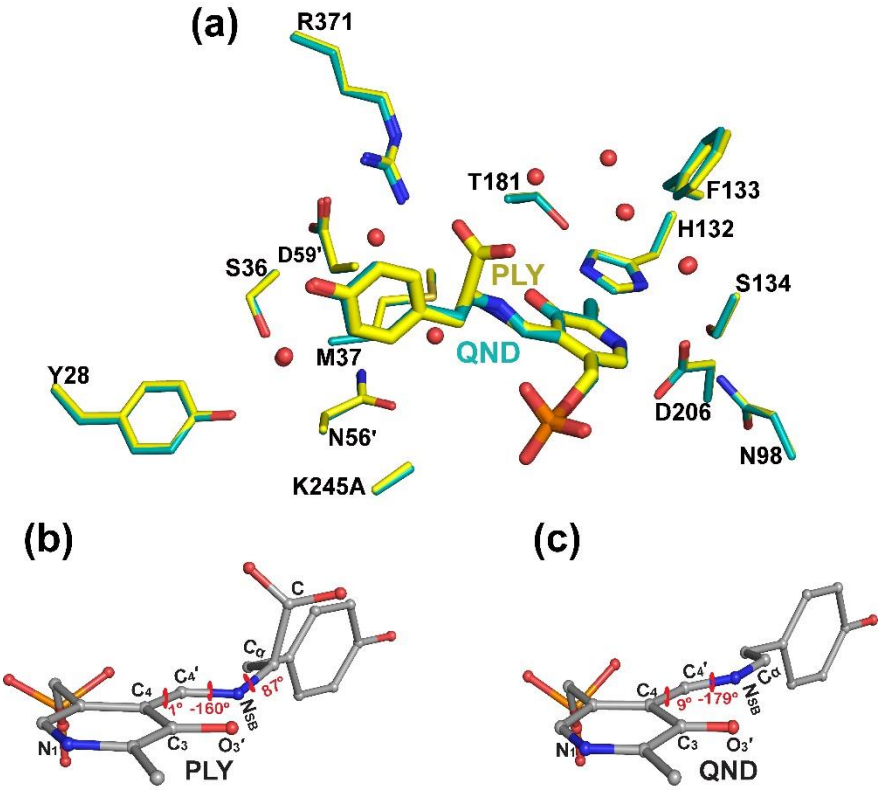

Figure 5. Geometry of PLY and QND. (a) Structural superposition showing identical interactions in the active site of PLY-K245A (yellow) and QND-K245A (teal). The side chain residues involved in cofactor binding, the ligands PLY and QND are represented in stick format. Water molecules are shown as red spheres. There is no significant conformational change in the active-site residues between the two forms. The geometry of both PLY and QND (grey ball-and-stick in panels (b), (c)) are consistent with the Dunathan hypothesis [2]. Panel (b) shows PLY in the Dunathan alignment. The C-Cα-N_{SB}-C4′, Cα-N_{SB}-C4′-C4 and N_{SB}-C4′-C4-C3 torsion angles (shown as red arcs) are 87°, -160° and 1°, respectively and are labelled in red. Panel (c) shows the quinonoid like QND ligand with Cα-N_{SB}-C4′-C4 and N_{SB}-C4′-C4-C3 torsion angles (shown as red arcs) of -179° and 9°, respectively.

Reorientation of conserved Arg371 is required for stabilization of the Dunathan intermediate

Given the structures, the next question was to explain how the Dunathan-alignment is favored in decarboxylases. In PLP-enzymes that catalyze the deprotonation reaction, for instance, in the tyrosine phenol lyase (TPL), the Dunathan-alignment of the leaving group proton is usually enforced by a salt bridge between the substrate-carboxylate and a conserved arginine (Arg371 in MjDC) (Figure 6a, b) [1,8]. However, in decarboxylases, an equivalent salt bridge can be a high-barrier interaction for the release of the labile carboxylate [29]. Mechanistic studies on homologous decarboxylases such as DGD also indicate that the Arg (specifically the positive charge) directly participates in the decarboxylation reaction, and influences substrate binding [13,30,31]. To the best of our knowledge, none of the ligand-bound decarboxylases available in the PDB to date demonstrate the Dunathan-alignment with the complete cognate ligand (Table S1). Hence, it has been challenging to identify the residues involved in enabling the alignment in decarboxylases, and decipher the molecular basis of how a structurally conserved arginine can choose one role over the other in two different reactions (Figure 6b) [1,6,29]. A comparison of the active-sites of the internal aldimine (holoMjDC•LLP) and the external aldimine (PLY-K245A) states of the enzyme serves to explain this conundrum (Figure 3a, c, Scheme 2-I/II).

In holoMjDC•LLP, the conformation of Arg371 appears conducive for a potential salt bridge with PLY-carboxylate (Figure 6c). This conformation is stabilized by interactions between Ser362 (Oγ) and Arg371 (Nε), and the backbone carbonyls of Thr181 and Gly35 with Arg371 (Nη1 and Nη2, respectively). In contrast, in the PLY-K245A, QND-K245A and apoMjDC•PLP_{ALD} forms, the Arg371 guanidinium group is present in a different conformation, (relative rotation ~87° along χ4), with the Nε and Nη2 atoms stabilized by interactions with the backbone carbonyl of Thr181, and the Nη1 atom with Oγ of Ser362. Interestingly, this reorientation of Arg371 sidechain precludes a salt bridge with the PLY-carboxylate (Figure 6c and Scheme 2-I/II). The rearrangement occurring in concert with a set of conserved changes due to the tilt of the pyridine-

ring is most likely influenced by the multiple hydrogen bonding interactions of the Arg side chain with the neighboring residues, namely, Ser362 and Thr181, and is common to the three structures (Figure 6b, c) [18]. This conformational switch between the holoMjDC•LLP form and all the successive forms is instrumental in forming a binding pocket for water molecule (W_C) in the corresponding active sites (Figure 6c). The presence of this water molecule is validated by its persistent residual density in the omit map, even at 5σ, and by its conservation in two independent subunits of the WT apoMjDC•PLP_{ALD} structure determined in a different crystal space group (PDB ID: 3F9T). Although a water molecule making interactions with the equivalent atom of carbiDOPA is also present in the structure of pig DDC bound to the inhibitor (PDB ID: 1JS3, chain A, HA1003, adjacent to Arg447), this water-mediated interaction with the ligand carboxylate was overlooked in the mechanism of DDC [27]. We propose that the W_C mediated interaction between Arg371 and the PLY-carboxylate occurs only in the activated state of the enzyme and most likely facilitates the carboxylate orientation of the indispensable Dunathan-alignment in decarboxylases. Chemical intuition suggests that only charged/small residues at this position would effectively/partially bind W_C and it is perhaps W_C that directly affects catalysis by stabilizing the Dunathan-alignment and modulating the electronic configuration of PLY. This is consistent with kinetic data of the equivalent R406M/K mutants in DGD, demonstrating that the positive charge of R406 is vital for both substrate binding and catalysis [12,13].

Given the subtle, but critical role of Arg371 in the reaction mechanism, we generated the R371A mutant of MjDC to examine the effect on activity. However, the variant displayed only a 7-fold decrease in activity, suggesting the loss of the Arg interactions can be compensated for by other interactions (Figure 1b). To identify these features, the structure of the R371A variant was determined to 2.1 Å resolution (Table 1). The two terminal residues and residues (275–278) part of the CL were disordered and not modelled in the structure. Continuous electron density was observed between PLP and the SB residue Lys245, consistent with internal aldimine formation (Figure 6d). Hence, the structure is termed as holoR371A•LLP. The structure of holoR371A•LLP and that of the active site residues are largely identical to the other structures (Table 2). Interestingly, in the mutant, two water molecules were found to occupy positions equivalent to that of the guanidinium group of Arg in holoMjDC•LLP (Figure 6d). Although neither of the water molecules corresponds to the exact position of W_C, it is to be noted that holoR371A•LLP is that of the LLP form where W_C is absent. Perhaps during the reaction, these water molecules in the variant can play the role of W_C, albeit with lesser efficiency (Figure 6).

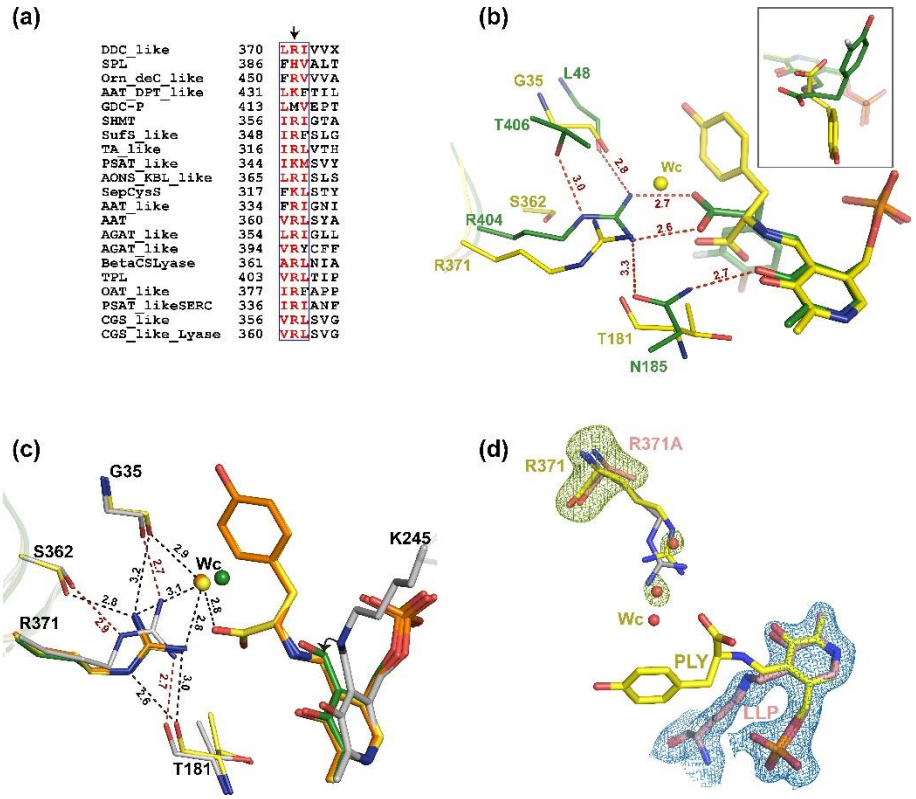

Figure 6. Role of Arg371 in decarboxylation. (a) Structure based sequence alignment of a representative set of proteins belonging to the different subfamilies of the fold-type I superfamily (Conserved Domain Database, CDD) [57]. The boxed residues highlight conservation of the region around arginine (Arg371 in MjDC) in the superfamily. (b) Superposition of the active sites of PLY-K245A (yellow sticks) and the homolog tyrosine phenol lyase (TPL, PDB ID: 2YCN, chain B, green sticks). Only one conformation of the bound 3-fluoro-L-tyrosine quinonoid of TPL is shown for clarity. In TPL the carboxylate group of the quinonoid makes a salt bridge with the structurally equivalent R404 residue [16]. Hydrogen bond interactions (in Å) are shown as dashed lines. Inset shows that the carboxylate group in PLY-K245A is aligned orthogonal to the pyridine ring of PLP whereas it is along the plane of the ring in TPL, consistent with the deprotonation reaction in TPL. (c) Superposition of the active site residues demonstrate different geometries of interaction of R371 and the conserved water (W_C) between the structures**.** Arg371 and the corresponding ligands of holoMjDC•LLP (PDB ID: 6JY1) [18], PLY-K245A, QND-K245A and and apoMjDC•PLP_{ALD} (PDB ID: 3F9T) are shown in grey, yellow, orange and green stick representation, respectively. Water is shown as spheres.The relative tilt of the pyridine ring between LLP and all other intermediates is represented by a black arrow. Hydrogen bond interactions (in Å) are shown as black dashed lines for PLY-K245A and red dashed lines for holoMjDC•LLP. (d) Superposition of the active site residues between holoMjDC•LLP (grey), PLY-K245A (yellow, with W_C) and holoR371A•LLP (pink) demonstrate that the two water molecules in holoR371A•LLP occupy the position equivalent to that of the guanidinium group of Arg371. Omit map (contoured at 2.8 σ) of R371A and the two water molecules in the active site residues are shown as green mesh. 2Fo−Fc map (contoured at 1.5 σ) of the internal aldimine of holoR371A•LLP is shown as blue mesh. Arg371, R371A, LLP and PLY are shown in stick format. Waters are shown as red spheres.

Thus, while Arg371 appears to play a crucial role in substrate recognition and binding before external aldimine formation, its structural rearrangement coupled with a water-mediated interaction is imperative to optimize the Dunathan-alignment and permit the neutral CO_2 to escape [13,29,32]. In the absence of this rearrangement, Arg371 can form a favorable salt-bridge interaction with the carboxylate instead and stall/alter the reaction. The subtle rearrangement is influenced by modifications in the hydrogen bonding interactions of the Arg side chain with the neighboring Gly34, Thr181 and Ser362 residues (Figure 6b, c). The interaction of Arg371 with the main chain carbonyls of Thr181, and Gly34 is preserved across homologous decarboxylases, whereas that with the side chain of Ser362 is distinct in the family, suggesting that the latter interaction could be involved in modulating the rate of decarboxylation across homologs (PDB ID: 1JS3, 1JS6, 4E1O, 4OBV, 6EEM) [18,25,27,28,33]. Thr181 is a conserved residue and part of an extended hydrogen bonding network implicated in modulating the stereoelectronic profile of the cofactor in Group II decarboxylases, and Gly34 belongs to the loop that shapes the substrate binding cavity [18]. The conservation of the Arg interactions implies that reaction specificity is directly related to the nature of the bound substrate and the electronic configuration of the Dunathan-intermediate. Similar interactions with the equivalent Asn and Leu residues are observed in TPL, suggesting that this phenomenon is perhaps common to the superfamily (Figure 6b, Figure S7). Hence, only the true substrates in the activated conformation can cause the rearrangement of the Arg residue with concomitant binding of Wc for reaction progress in decarboxylases. This is consistent with the mechanistic studies in DGD with alternate substrates [12].

These snapshots of MjDC highlights how evolution has economically permuted the conformational landscape of a single conserved Arg residue to favor the decarboxylation reaction over others, and how subtle modifications in the active site micro-environment lead to significant modulation of reaction rate and specificity patterns across homologous members of the superfamily (Figure 6). For instance, in AAT, the substitution of the structurally equivalent Arg to Lys suppresses transamination, and enhances β-decarboxylation [34]. The potential effects of substitutions of Arg371 on side-reactions of MjDC remains to be examined.

A conserved extended hydrogen-bonding network likely influences rate of decarboxylation

Another feature that affects the rate of PLP-dependent reactions is the protonation states of the N1 and N_{SB} atoms. Protonated N1 and N_{SB} (PSB) atoms of the external-aldimines of fold-type I

enzymes promote catalysis by stabilizing Cα-carbanions *via* ylide-type interactions [4,6,29,35,36]. Therefore, in our study, the geometry of the refined PLY model corresponds to the protonated N1 form of zwitterionic-PSB (Figure S8) (see Experimental Procedures). In this case, we envisage a state where W_C may stabilize/neutralize the charge on the carboxylate facilitating decarboxylation of the zwitterionic tautomer [29]. Subsequent electron delocalization from the Cα would assist in overcoming the recombination of the electrophilic CO_2 with the Cα-carbanion, thereby influencing the decarboxylation rate [37, 38]. Indeed, the PSB tautomer is favored when a neutral group (methyl-aldimine) is substituted for L-DOPA-aldmine in DDC [36]. Additionally, the tautomeric equilibrium between the zwitterionic and neutral forms of the Schiff base aldimines is influenced by intra-molecular proton transfers through hydrogen-bonding networks present in the active site [36, 37]. In a previous comparative analysis of apo and LLP forms of MjDC and homologs, we had identified a conserved extended hydrogen bonding network that connects the N1, N_{SB} and O3′ atoms and proposed that this network of catalytic residues may profoundly influence the protonation states of these atoms. Disruptions of the network using substitution mutants resulted in significant disruption of activity (Figure S9) [18]. Interestingly, in the PLY complex, the carboxylate makes multiple interactions with this network (Figure 7a). It is tempting to speculate that after the Dunathan-alignment is achieved, the interactions of the labile carboxylate through this network may be coupled to the protonation profiles of N1, N_{SB} and O3′, thereby modulating the electronic properties of PLY towards forming the stable quinonoid/carbanion and efficient catalysis [4,6,35].

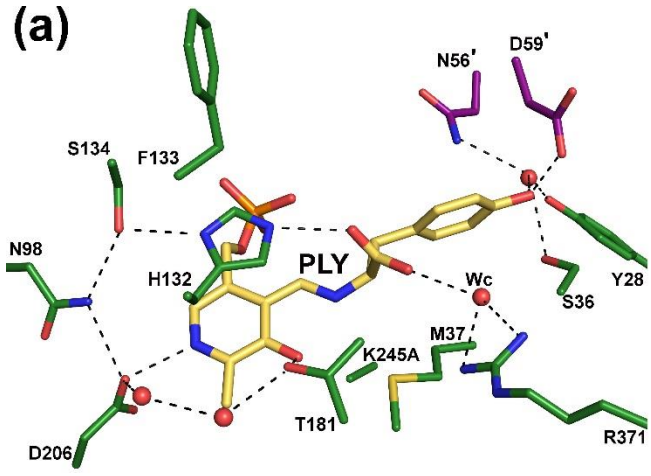

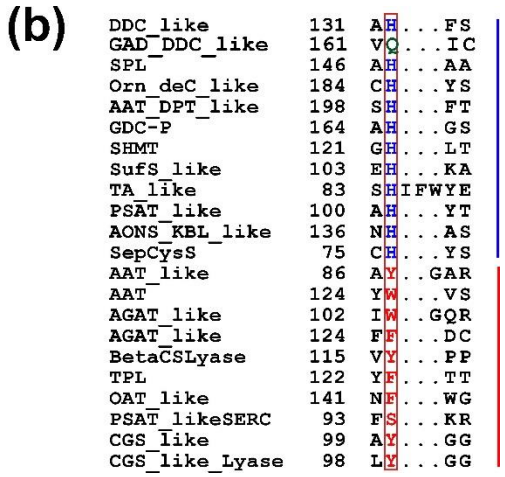

Figure 7. The conserved extended hydrogen-bonding network is coupled to the leaving Cα-carboxylate. (a) The PLY ligand was docked in the active site of apoMjDC•$PLP_{ALD.}$ A close up view of the active site shows that the PLY-carboxylate is connected to the N1-PLP and the O3' through the conserved extended hydrogen-bonding network through His132, Ser134, Asn98, Asp206, two water molecules and Thr181 [18]. Side chains and ligands are represented in stick format. Residues from one subunit are colored in green, and the second subunit in puple, and PLY in yellow. Water is shown as red sphere. Hydrogen bond interactions (< 3.2 Å) are shown as dashed lines. (b) Structure-based sequence alignment of a representative set of proteins belonging to the different subfamilies of the fold-type I superfamily. The red-boxed residues highlight conservation of the His (His132 in MjDC, blue) in subfamilies that can catalyze decarboxylation reactions, whereas it is replaced with tyrosine, tryptophan or phenylalanine in subfamilies that catalyze transamination. An infrequent histidine to glutamine substitution is also seen in bacterial decarboxylases of the Group II decarboxylase subfamily and is shown in green.

Protonation of the quinonoid intermediate (QND-Cα) for productive amine formation

The final step in the reaction is the poorly-described quinonoid-Cα protonation [9,10,23,24,25]. Protonation of QND-Cα happens on the *re* face of the intermediate that is solvent-exposed in both K245A-intermediate complexes, deterring the direct identification of the residue required for this function. Previous biochemical and computational studies on homologs indicate an indispensable catalytic role for the highly conserved Tyr273′ residue present in the CL of the adjacent subunit [9,18,23,24,25]. The composition and length (13-24 residues) of the CL region are divergent across orthologs. Moreover, the CL is known to be dynamic and is usually disordered in crystal structures of Group II decarboxylases and is believed to play a role in the open-to-closed transitions occurring between multiple states of the catalytic cycle [9,18,23,24,25,28,38,39,40,41]. Due to the absence of relevant structural snapshots, the identity of the residue remains debated [9,11,28]. For example, biochemical studies of some homologs indicate that the neighboring conserved His132 residue can also acts as a potential proton donor [10,11,27,28,42]. The CL regions of PLY-K245A and QND-K245A are also disordered (Figure 2a, b) [18,23]. Incidentally, the CL of apoMjDC•PLP_{ALD} is in an ordered, "closed" CL conformation identical to that reported in three other ligand-bound homologs and described in detail in our previous study (Figure 8a, Table S1) [18]. Therefore, we reconstructed the closed-form CL pose for the two reaction-intermediate structures by superposing these onto the structure of apoMjDC•PLP_{ALD}. In this model, the structural arrangement upon active site closure positions the Tyr273′-OH at ~7 Å from PLY/QND–Cα atom and 4.4 Å from His132 (Nε2), however too far away for direct protonation. Tyr273′ is stabilized in a strained *gauche* conformation by a conserved hydrogen bond with the backbone amide of a neighboring Phe133 (Figure 8b). Interestingly, a functionally-implicated water (W1) of the extended hydrogen-bonding network is present in apoMjDC•PLP_{ALD}, located at a position equivalent to the PLY-carboxylate OT2 atom [18]. W1 is positioned at 2.9 Å from the anticipated PLY/QND–Cα atom and at 3 Å from His132 (Nε2) (Figure 8b).

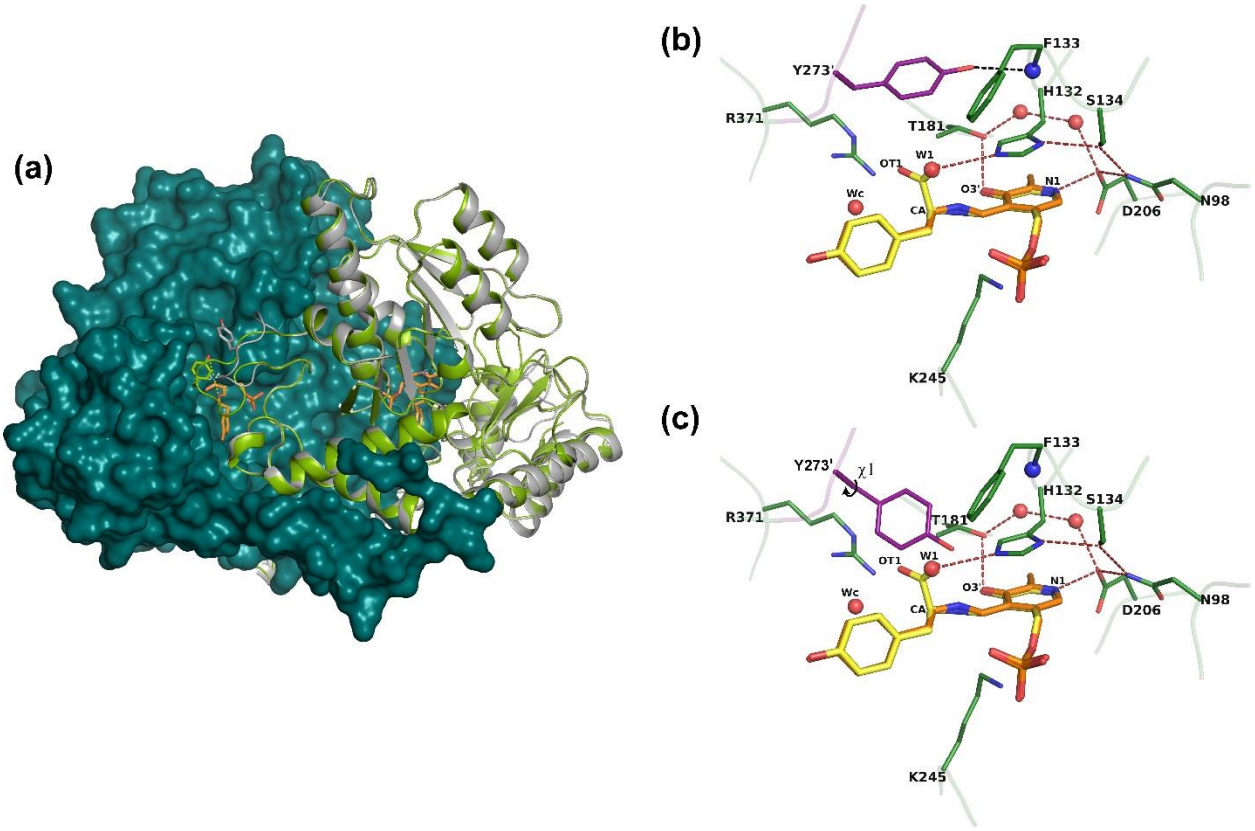

Figure 8. Model of protonation of the quinonoid intermediate. (a) Open and closed conformations of wild-type MjDC. One subunit of the dimer is shown in surface representation (teal). PLY ligand (orange sticks) from PLY-K245A is docked in the active site cavity of apoMjDC•PLP_{ALD} (PDB ID: 3F9T). The other subunit of apoMjDC•PLP_{ALD} (green ribbon representation) shows the "closed" CL conformation. The corresponding subunit of holoMjDC•LLP (grey ribbon) (PDB ID: 6JY1) represents the "open" CL conformation. Tyr273′ of the CL is represented in stick format and highlights the closed-to-open transition of the CL between the two structures. The distance between Tyr273′ and the Cα of the docked PLY ligand is shown as a yellow dashed line [18]. Panels (b) and (c) are close-up views of the active site interactions in the "closed" CL model. The PLY (yellow sticks) and QND (orange sticks) ligands were positioned into the active site of apoMjDC•PLP_{ALD} by superposition of PLY-K245A and QND-K245A, respectively. Residues in the active site of one subunit are shown as green stick representation while the catalytic Tyr273′ of the adjacent subunit is represented in purple. The OT2 atom of PLY is at a position equivalent to W1 present in apoMjDC•PLP_{ALD}. OT2 in PLY and W1 in apoMjDC•PLP_{ALD} make hydrogen bonding interactions with the conserved extended hydrogen-bonding network (red dashed lines). (b) The conserved hydrogen bond (black dashed line) between Tyr273′-OH and Phe133 main chain amide (blue sphere) is shown. The distances between the Tyr273′-OH and His132 (Nε2), W1 and the anticipated QND-Cα (labelled as CA) atoms are 4.4 Å, 5.5 Å and 7.1 Å, respectively. In this model, Tyr273′ can protonate QND-Cα *via* W1 and His132 (Scheme 2, IIIB) (c) A model where Tyr273′ undergoes a minor reorientation *via* a rotation around its χ1 torsion angle (indicated by a black arrow) to bring Tyr273′-OH, W1 and His132 (Nε2) atoms to within 3.2 Å of each other. In this scenario, Tyr273′ can directly protonate QND-Cα (Scheme2, IIIA).

Accordingly, two scenarios can be envisaged involving Tyr273′ as a proton donor at the end of the decarboxylation process after CL closure. In scenario A, a minor reorientation of the Tyr side-chain to an ideal *gauche* conformation can displace W1 and position Tyr273′-OH close enough

(< 3.5 Å) for direct proton transfer to QND–Cα. (Figure 8c and Scheme 2-IIIA). This scenario is based on the hypothesis proposed for the direct involvement of the Tyr273′ residue in human HDC and GAD [24,25]. However, several other studies suggest that the conserved His132 at the active site is the likely proton donor acting either *via* a catalytically active water molecule or in concert with Tyr273 [9,11,27,28,42]. In this context, an alternate scenario B is proposed where Tyr273′, in its originally observed conformation can mediate protonation of QND–Cα using water W1 (Figure 8b, Scheme 2-IIIB). First, this geometry is consistent with biochemical data supporting a direct role of His132 in proton transfer by promoting the alignment of W1 and the stereoelectronic modulation of QND through hydrogen bonding. Second, the geometry and location of W1 adjacent to QND–Cα also explains how this arrangement can stabilize the Cα-carbanion over C4′-carbanion to favor productive-protonation over abortive-transamination (Scheme S1). Scenario B is also in good agreement with the observed relative activity patterns of MjDC substitution mutants, namely, H132A (1.2%), H132Q (94%), and Y273F (undetectable under assay conditions) (Figure 1b). Y273 is completely conserved while the H132Q substitution infrequently occurs across homologous decarboxylases (Figure 7b) [18]. Interestingly, a QM/MM study on the homologous HDC proposes a model where quinonoid Cα protonation mediated by water at a position equivalent to that of W1 is more favorable than direct protonation by Tyr [9]. Moreover, a recent study on plant aromatic amino acid decarboxylases proposed a model where the equivalent Tyr and His residue interactions facilitates proton transfer from the Tyr residue to the carbanionic quinonoid intermediate [28]. Our structural data allows us to propose a mechanistically similar model that takes into account interactions between the Tyr273′ and the extended hydrogen bonding network including W1, and the conserved His132, that together participate in the protonation of the quinonoid intermediate without perturbing the frequently observed conformation of the Tyr residue (Figure 8, Scheme 2). Finally, both scenarios presume that the release of CO_2 from the active-site facilitates stable CL closure.

In summary, two cognate reaction intermediates, in productive modes for catalysis, were obtained *in-crystallo* within a single enzyme for the first time in a PLP-dependent decarboxylase. These structures together with those of the PLP bound form, the R371A variant, and the apo- and holo-forms of the wild-type, and complemented by activity data, allow us to understand how control of reaction specificity and the subsequent protonation of the quinonoid, is enforced in a decarboxylase. Our results reveal hitherto undescribed cryptic structural features of decarboxylases that may not have been evident in the absence of these snapshots. The structures are a strong starting point to probe mechanistic details using QM/MM studies and in

the rational design of enzymes for altered functionality or to enable the design of better inhibitors for drug targets like DDC, a close homolog of MjDC. More so, the current study will help better understand the structural basis of the evolution of PLP-dependent enzymes that display such exquisite reaction specificity and substrate selectivity.

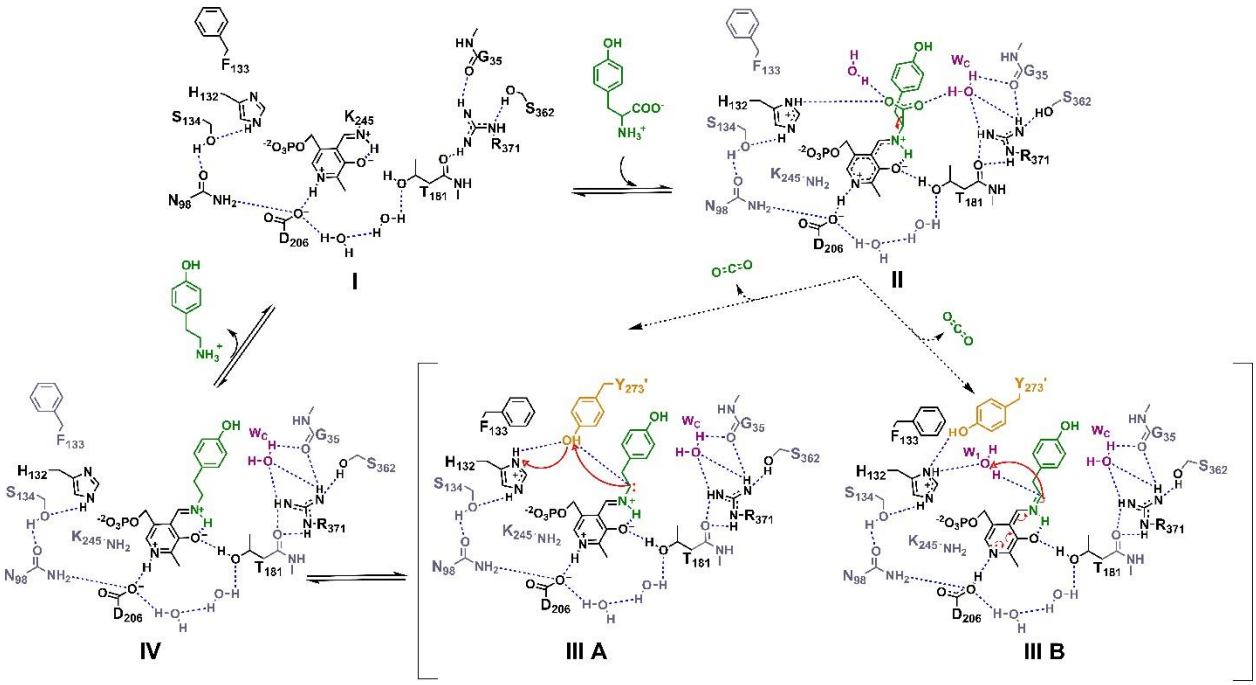

Scheme 2. Proposed mechanism of tyrosine decarboxylation by MjDC

EXPERIMENTAL PROCEDURES

Site-directed mutagenesis

pSpeedET vector containing *MJ0050* gene that encodes for MjDC (Uniprot Id Q60358) was purchased from DNASU (JCSG 390948; PSI: Biology Materials Repository Clone ID: MjCD00289364, http://psimr.asu.edu/) [17,43]. Oligonucleotides not listed in our previous study and used for mutagenesis in the current study are listed in Table S3 [18]. All mutations were confirmed by DNA sequencing.

Protein expression and purification

Wild type (WT) and the variants of MjDC were expressed in BL21-CodonPlus (DE3)-RIL cells (Agilent Technologies) and purified to homogeneity by thermal precipitation, followed by Ni^{2+} affinity chromatography as described previously [18]. The proteins were concentrated to ~40mg/ml and stored at -80°C. Protein concentration was estimated by UV absorption at 280 nm using a molar extinction coefficient of 34310 M^{-1} cm^{-1}. A HiPrep Sephacryl S-200 HR size-exclusion column (GE Healthcare, UK) on an AKTA FPLC system was used to determine the oligomeric status of K245A. Briefly, 2.0 mg/ml of K245A was loaded onto the column equilibrated with 100 mM HEPES buffer, pH 8.0 and eluted at a flow rate of 0.4 ml/min. The apparent molecular weight of K245A was compared with the elution volume of the WT protein under the same experimental conditions.

Spectral measurements in solution

Aldimine formation was detected by measuring spectral changes in WT and K245A in the presence of 100-fold excess of L-Tyr substrate in a solution containing 20 µM protein in 50 mM HEPES buffer, pH 8.0 and 100 µM DTT. The basal level spectra of the protein alone were measured for 20 scans and then the ligand was added. For the WT protein, wavelength change from the maxima observed in the basal level peak (~ 414 at 30 ºC/ 420 nm at 70 ºC) was monitored with respect to time to detect the reaction progress. Spectral scans were measured at 30 ºC and 70 ºC with the WT to monitor reaction progress. Appropriate blank spectra without the proteins were recorded and subtracted from the protein spectra. For the K245A mutant, change in peak height (~433 nm) with excess tyrosine and PLP was measured to detect formation of external aldimine at RT. Spectra of PLP and L-Tyr without the protein were monitored for the same time and used as blank to rule out the effect of non-enzymatic external aldimine formation. Each spectrum is an average of three spectral scans taken for a single time period. All absorption measurements were collected in a quartz cuvette of 1cm path length in a double beam UV-visible spectrophotometer (Perkin Elmer Lambda 25, USA). Temperature was controlled during the measurements with a Peltier temperature controller attached to the spectrophotometer at the specified temperatures.

Enzyme assays

Decarboxylase assay was performed with 10 µg of enzyme incubated with 0.5 mM L-Tyr and 20 µM PLP in 50 mM HEPES, pH 8.0 (final volume 250 µl), at 80°C for 5 min. The product tyramine was extracted in the organic layer (toluene) as a trinitrophenylamine derivative by incubating with

250 µl of 2, 4, 6-trinitrobenzesulfonic acid (TNBS) and 500 µl toluene for 1 h, as described by previously [18,44]. The concentration of trinitrophenyltyramine in toluene was measured at 340 nm with a multimode microplate reader (SpectraMax, Molecular Devices, USA). Experiments were performed in triplicates. GraphPad Prism 5.0 software was used for generating figures.

Crystallization, data collection and refinement of R371A, K245A and its ligand complexes

Crystals of the K245A and R371A variants were grown in identical conditions to that of holoMjDC•LLP by hanging-drop vapour diffusion method at 20 °C[18]. The volume of the reservoir solution (0.1 M sodium citrate pH 5.4, 0.2 M sodium potassium tartrate, 2.0 M ammonium sulphate) was 500 µl and the drop volume contained 1 µl of protein (~20 mg/ml) and 1 µl of reservoir solution. Attempts to obtain crystals of cognate substrate/product bound complexes with holoMjDC•LLP using extensive co-crystallization and soaking experiments proved unsuccessful. A possible explanation could be that MjDC does not undergo transaldimination at the crystallization pH of 5.4. This is further supported by the 10-fold decrease in enzyme activity at pH 5.0 reported in our previous study [18]. Crystals of the reaction-intermediate complexes were successfully obtained by soaking K245A crystals with excess PLP and the ligands. X-ray diffraction data for K245A (apoK245A, data not shown), K245A soaked with PLP (PLP-K245) and K245A soaked with L-Tyr (PLY-K245A) were collected from single crystals in cyro-protectant (2.0 M ammonium sulphate and 40% glycerol) under cryo conditions (100 K nitrogen stream) at the BM14 beamline (European Synchrotron Radiation Facility, Grenoble, wavelength 0.91841 Å). Diffraction data for the QND-K245A (PLP-K245A crystals soaked with L-Tyr) and holoR371A•LLP were collected at home source under cryo conditions with a MAR345 image plate detector mounted on a Bruker MICROSTAR rotating anode X-ray generator (Cu Kα = 1.5418 Å). Unit cell parameters and space group for all the datasets essentially remained unchanged with holoMjDC•LLP (Table 1), therefore the ligands were located by difference Fourier techniques, following rigid-body and simulated-annealing refinement using holoMjDC•LLP (PDB ID: 6JY1) as the starting model. All four crystals had one molecule in the asymmetric unit. Electron-density maps were unambiguous for all the intermediate complexes with K245A and for LLP in holoR371A•LLP. Data collection statistics are given in Table 1. *PyMoL* was used for graphical representation of structures (The PyMOL Molecular Graphics System, Version 2.0 Schrödinger, LLC). All mFo−DFc omit maps were generated after restrained refinements using simulated annealing at 5000 K in *PHENIX* with a model lacking the atoms listed under each figure [45].

Stereo-chemical quality of the final models (PLP-K245A, PLY-K245A, QND-K245A and holoR371A•LLP) were evaluated using the *MolProbity* program [46].

Data collection and refinement of PLP-K245A

Crystals of the K245A variant were soaked with saturating concentrations of PLP with an intention to explore the potential of its active site in binding to cognate ligands. The Schiff base lysine variant has been used in several other instances to structurally capture the intermediates of PLP-dependent catalysis, although not for Group II decarboxylases [47,48,49,50]. The electron density map of PLP-K245A, solved at 1.79 Å clearly confirmed the presence of PLP in its aldehyde state (pyridoxal-P). Pyridoxal-P was modelled in two different conformations with 61% and 39% occupancies, refined using the *PHENIX* occupancy refine option [45]. In the difference mFo-DFc map of PLP-K245A, two electron density peaks were observed at the putative substrate binding region. An ammonium ion could be modelled with reasonable B factors (24 $Å^2$) near the Oδ2 atom of Asp59′ in the first peak, whereas the second unassigned density, appeared to resemble a tetrahedral oxoanion such as a phosphate/sulphate possibly interacting with the O4′ of pyridoxal-P. Both ions are a part of the crystallization mixture but refine with B-factors considerably higher than the average B-factors of adjacent residues, when modelled with full occupancy. Electron density maps of residues 268–278 (part of the CL) and the C-terminal loop region appears to be discretely disordered in all the structures with the K245A variant. This prevented accurate modelling and refinement of this region.

Data collection and refinement of PLY-K245A and QND-K245A

Data collected from PLP-K245A crystals at the synchrotron source from immediate flash freezing of crystals soaked with L-Tyr for 10 s and solved at 1.8 Å, showed that the active site was occupied with the an external-aldimine complex with tyrosine (PLY-K245A) with full occupancy. Interestingly, data collected using crystals soaked in L-Tyr at home source (solved at 1.9 Å), resulted in the capture of the post-decarboxylation, quinonoid-like intermediate (QND-K245A), enabling us to capture two consecutive steps of the decarboxylation reaction catalyzed by this enzyme. X-ray diffraction data were collected from multiple crystals that were exposed to different soaking conditions varying the substrate concentrations and soaking time. Most data were inconclusive owing to crystal damage or poor resolution where the electron density for the ligand was difficult to interpret due to disorder or poor binding. The QND-K245A structure presented

here is that from a successful data set that was obtained after 48 hrs of soaking. The soaking time is not indicative of the rate of the reaction *in-crystallo*.

Optimization of ligand geometries

Initial coordinates and restraints for PLY and QND were built using the *JLigand* module in *CCP4* suite [51]. The resolution of the X-ray diffraction data does not allow for the explicit modeling of hydrogen atoms to identify the protonation states of PLY present in the crystal. However, we explored the possibility of evaluating two possible protonation states of PLY for the best fit to the electron density maps. To this end, *PubChem Sketcher V2.4* was used to generate the SMILES files for two different protonation states of PLY, a) unprotonated-N1 and N_{SB} and b) protonated-N1, zwitterionic-PSB [52]. The corresponding restraints were then optimized using the AM1 semi-empirical quantum-chemical method and generated as a crystallographic information file (CIF). The two sets of coordinates and restraints were manually inspected for validity using the *Restraints Editor Especially Ligand (REEL)* tool in *PHENIX* suite [53]. Refinement was carried out in *PHENIX* using both sets of PLY restraints for the PLY-K254A structure and the 2mFo-DFc maps and the mFo-DFc difference maps were carefully examined for evidence of positive/negative densities. Two positive difference density peaks at 3.6 σ and 4.2 σ were observed around the unprotonated N1 and N_{SB} atoms of PLY, respectively, whereas the corresponding peak heights for the protonated N1 and zwitterionic PSB atoms were at 2.3 σ and 3.6 σ, respectively. Therefore, the model of PLY that resulted in the relatively flat mFo-DFc map (the protonated-N1, zwitterionic-PSB form of PLY) was fitted in the electron density maps of PLY-K245A (Figure S8 A, B). Inference of the protonation states from the crystallographic data is unreliable here given the resolution. However, the protonation state of the final model here is consistent with the prevalent state deduced using previous NMR, neutron diffraction and computational studies of external aldimines of fold type-I enzymes [29,35,54,55]. An identical optimization and refinement protocol was performed for the QND intermediate. We have modelled QND with a protonated N1 and zwitterionic PSB in QND-K245A, consistent with the PLY ligand. We believe that our protonation state models, although largely speculative, can serve as better starting models for further rigorous QM/MM studies.

Characterization of crystals

In order to estimate the catalytic competence of the PLP-K245A crystals, UV–visible absorption spectra were collected from crystals soaked in L-Tyr for different time periods. Spectral scans of

the crystals were collected in capillary tubes of 1mm path length in the diffusive reflectance spectroscopic apparatus of a Lambda 950 UV-VIS-NIR spectrophotometer (Perkin Elmer, USA). Spectra from the empty capillary tubes were used for baseline correction. Blank spectra were collected from PLP-K245A crystals in identical conditions but not subjected to the soaking experiment with the substrate.

Electron Spray Ionization Mass Spectrometry (ESI-MS) was performed on crystal samples to analyze the nature of intermediates present in the crystals. After soaking in PLP and L-Tyr, the PLY-K245A crystals were washed thoroughly in mother liquor and resuspended in water. The samples were desalted using C18 Zip-Tips (*Millipore, Ireland*) and infused directly into the ESI source of an Orbitrap Elite Mass spectrometer (*Thermo, Germany*) operating in the positive ion mode. The MS data were acquired over the m/z range of 200–1000 continuously. Spectra collected from PLP and L-Tyr without the crystals in identical conditions was used as reference for the identification of unique peaks of the intermediates formed in the crystal.

Sequence and structural alignment of fold type-I enzymes

The alignment was based on a structural superposition using holoMjDC•LLP (PDB ID: 6JY1) as the template and was generated using Dali Lite v.3. ESPRIPT 3.0 (http://espript.ibcp.fr/ESPript/cgi-bin/ESPript.cgi) was used to generate the sequence alignment figure [56]. The protein sequences used for structure based sequence analysis are DDC_like (DOPA dearboxylase like family, PDB ID: 6JY1, tyrosine/aspartate decarboxylase), GAD_DDC_like (DOPA dearboxylase like family, PDB ID: 1XEY, glutamate decarboxylase), Orn_dec_like (Ornithine_decarboxylase like family, PDB ID: 2JIS, cystenie sulfinic acid decarboxylase), GDC-P (Glycine decarboxlase-P family, PDB ID: 1WXU, Glycine decarboxlase-P subunit), SHMT (Serine hydroxyl methyl transferase family, PDB ID: 1YJZ, Serine hydroxyl methyl transferase), SufS_like (cysteine desulfurase_like family, PDB ID: 3LVL, cysteine desulfurase), TA_like (threonine_aldolase family, PDB ID: 1JG8, low specificity threonine_aldolase), PSAT_like (phosphoseryl aminotransferase family, PDB ID: 3WKS, SepCysS-SepCysE N-terminal domain), AOS_like (α-oxoamine synthases_like family, PDB ID: 5VNX, 8-amino-7-oxononanoate synthase), SepCysS (Sep-tRNA:Cys-tRNA synthase family, PDB ID: 2E7J, Sep-tRNA:Cys-tRNA synthase), AAT_like (aspartate aminotransferase like family, PDB ID: 1M32, 2-aminoethylphosphonate Transaminase), AAT (aspartate aminotransferase family, PDB ID: 1GC4, aspartate aminotransferase), AGAT_like (alanine glyoxalate transferase like family, PDB ID: 3IMZ, alanine glyoxalate transferase), BetaCSLyase (cystathionine beta-

lyase family: , PDB ID: 3B1E, beta C-S lyase), TPL (beta-eliminating lyase family, PDB ID: 2YCN, tyrosine phenol lyase), OAT_like (acetyl ornithine aminotransferase like family, PDB ID: 1OAT, ornithine aminotransferase), CGS_like (cystathionine gamma-synthase like family, PDB ID: 3QHX, cystathionine gamma-synthase MetB) and CGS_like_Lyase (cystathionine gamma-synthase_like family, PDB ID: 4IYO, cystathionine gamma-lyase).

Accession codes

Coordinates and structure factor data for PLP-K245A, PLY-K245A, QND-K245A and holoR371A•LLP have been deposited in the PDB with the accession codes 6LDR, 6LDS, 6LDT and 6M4Y, respectively.

AUTHOR CONTRIBUTIONS

SCG carried out the experiments and analyzed the data. NM carried out data analysis, supervised the study and wrote the manuscript jointly with SCG

FUNDING SOURCES

SCG is supported by funding from the Council of Industrial and Scientific Research (CSIR) and the Ministry of Human Resource and Development (MHRD), Government of India.

NOTES

The authors declare that they have no conflicts of interest with the contents of this article.

ACKNOWLEDGMENTS

We thank Babu A. Manjasetty for help with data collection at BM14 beamline (ESRF, Grenoble), funded by the BM14 project, Department of Biotechnology (DBT) India, ESRF and EMBL. The Macromolecular X-ray Diffraction Facility, the Sophisticated Analytical Instrumentation Facility and the DST-FIST Facility at IIT Madras are acknowledged.

1

REFERENCES

1. Dunathan, H. C. (1966). Conformation and reaction specificity in pyridoxal phosphate enzymes. *Proc. Natl. Acad. Sci. USA* **55**, 712-6.
2. Dunathan, H. C. (1971). Stereochemical Aspects of Pyridoxal Phosphate Catalysis. *Adv. Enzymol. Relat. Areas Mol. Biol.,* **35**, 79-134.
3. Schneider, G., Kack, H. & Lindqvist, Y. (2000). The manifold of vitamin B6 dependent enzymes. *Structure* **8**, R1-6.
4. Toney, M. D. (2005). Reaction specificity in pyridoxal phosphate enzymes. *Arch. Biochem. Biophys.* **433**, 279-87.
5. Richard, J. P., Amyes, T. L., Crugeiras, J. & Rios, A. (2009). Pyridoxal 5'-phosphate: electrophilic catalyst extraordinaire. *Curr. Opin. Chem. Biol.* **13**, 475-83.
6. Toney, M. D. (2011). Controlling reaction specificity in pyridoxal phosphate enzymes. *Biochim. Biophys. Acta, Proteins Proteomics* **1814**, 1407-1418.
7. Toney, M. D. (2014). Aspartate aminotransferase: an old dog teaches new tricks. *Arch. Biochem. Biophys.* **544**, 119-27.
8. Dajnowicz, S., Parks, J. M., Hu, X., Johnston, R. C., Kovalevsky, A. Y. & Mueser, T. C. (2018). Hyperconjugation Promotes Catalysis in a Pyridoxal 5′-Phosphate-Dependent Enzyme. *ACS Catal.* **8**, 6733-6737.
9. Fernandes, H. S., Ramos, M. J. & Cerqueira, N. M. (2017). The Catalytic Mechanism of the Pyridoxal-5′-phosphate-Dependent Enzyme, Histidine Decarboxylase: A Computational Study. *Chem. - Eur. J.* **23***,* 9162-9173.
10. Ni, J., Xu, G., Dai, W., Zhao, Y.-L. & Ni, Y. (2019). Hyperconjugation promoted by hydrogen bonding between His98/His241 and a carboxyl group contributes to tyrosine decarboxylase catalysis. *Catal. Sci.Tech.* **9**, 6222-6226.
11. Liang, J., Han, Q., Tan, Y., Ding, H. & Li, J. (2019). Current Advances on Structure-Function Relationships of Pyridoxal 5'-Phosphate-Dependent Enzymes. *Front. Mol. Biosci.* **6**, 4.
12. Sun, S., Zabinski, R. F. & Toney, M. D. (1998). Reactions of alternate substrates demonstrate stereoelectronic control of reactivity in dialkylglycine decarboxylase. *Biochemistry* **37**, 3865-75.
13. Fogle, E. J. & Toney, M. D. (2010). Mutational analysis of substrate interactions with the active site of dialkylglycine decarboxylase. *Biochemistry* **49**, 6485-93.
14. Szebenyi, D. M., Liu, X., Kriksunov, I. A., Stover, P. J. & Thiel, D. J. (2000). Structure of a murine cytoplasmic serine hydroxymethyltransferase quinonoid ternary complex: evidence for asymmetric obligate dimers. *Biochemistry* **39**, 13313-13323.
15. Barends, T. R., Domratcheva, T., Kulik, V., Blumenstein, L., Niks, D., Dunn, M. F. & Schlichting, I. (2008). Structure and mechanistic implications of a tryptophan synthase quinonoid intermediate. *Chembiochem* **9**, 1024-1028.
16. Milic, D., Demidkina, T. V., Faleev, N. G., Phillips, R. S., Matkovic-Calogovic, D. & Antson, A. A. (2011). Crystallographic snapshots of tyrosine phenol-lyase show that substrate strain plays a role in C–C bond cleavage. *J. Am. Chem. Soc.* **133**, 16468-16476.
17. Kezmarsky, N. D., Xu, H., Graham, D. E. & White, R. H. (2005). Identification and characterization of a L-tyrosine decarboxylase in Methanocaldococcus jannaschii. *Biochim. Biophys. Acta* **1722**, 175-82.

18. Chellam Gayathri, S. & Manoj, N. (2019). Structural insights into the mechanism of internal aldimine formation and catalytic loop dynamics in an archaeal Group II decarboxylase. *J. Struct. Biol*. **208**, 137-51.
19. Nishino, J., Hayashi, H., Ishii, S. & Kagamiyama, H. (1997). An Anomalous Side Reaction of the Lys303 Mutant Aromatic L-Amino Acid Decarboxylase Unravels the Role of the Residue in Catalysis. *J. Biochem.* **121**, 604-11.
20. Bertoldi, M. & Voltattorni, C. B. (2009). Multiple roles of the active site lysine of Dopa decarboxylase. *Arch. Biochem. Biophys.* **488**, 130-9.
21. Moore, P. S., Bertoldi, M., Dominici, P. & Borri Voltattorni, C. (1997). Aromatic amino acid methyl ester analogs form quinonoidal species with Dopa decarboxylase. *FEBS Lett.* **412**, 245-8.
22. Bertoldi, M., Cellini, B., Maras, B. & Voltattorni, C. B. (2005). A Quinonoid is an Intermediate of Oxidative Deamination Reaction Catalyzed by Dopa Decarboxylase. *FEBS Lett.* **579**, 5175-80.
23. Bertoldi, M. (2014). Mammalian Dopa Decarboxylase: Structure, Catalytic Activity and Inhibition. *Arch. Biochem. Biophys.* **546**, 1-7.
24. Fenalti, G., Law, R. H., Buckle, A. M., Langendorf, C., Tuck, K., Rosado, C. J., Faux, N. G., Mahmood, K., Hampe, C. S., Banga, J. P., Wilce, M., Schmidberger, J., Rossjohn, J., El-Kabbani, O., Pike, R. N., Smith, A. I., Mackay, I. R., Rowley, M. J. & Whisstock, J. C. (2007). GABA Production by Glutamic Acid Decarboxylase is Regulated by a Dynamic Catalytic Loop. *Nat. Struct. Mol. Biol.* **14**, 280-6.
25. Komori, H., Nitta, Y., Ueno, H. & Higuchi, Y. (2012). Structural study reveals that Ser-354 determines substrate specificity on human histidine decarboxylase. *J. Biol. Chem.* **287**, 29175-83.
26. Giardina, G., Montioli, R., Gianni, S., Cellini, B., Paiardini, A., Voltattorni, C. B. & Cutruzzolà, F. (2011). Open conformation of human DOPA decarboxylase reveals the mechanism of PLP addition to Group II decarboxylases. *Proc. Natl. Acad. Sci. USA* **108**, 20514-20519.
27. Burkhard, P., Dominici, P., Borri-Voltattorni, C., Jansonius, J. N. & Malashkevich, V. N. (2001). Structural insight into Parkinson's disease treatment from drug-inhibited DOPA decarboxylase. *Nat. Struct. Mol. Biol.* **8**, 963-967.
28. Torrens-Spence, M. P., Chiang, Y. C., Smith, T., Vicent, M. A., Wang, Y. & Weng, J. K. (2020). Structural basis for divergent and convergent evolution of catalytic machineries in plant aromatic amino acid decarboxylase proteins. *Proc. Natl. Acad. Sci. USA* **117**, 10806-10817.
29. Bach, R. D., Canepa, C. & Glukhovtsev, M. N. (1999). Influence of Electrostatic Effects on Activation Barriers in Enzymatic Reactions: Pyridoxal 5‘-Phosphate-Dependent Decarboxylation of α-Amino Acids. *J. Am. Chem. Soc.* **121**, 6542-6555.
30. Tan, D., Harrison, T., Hunter, G. A. & Ferreira, G. C. (1998). Role of Arginine 439 in Substrate Binding of 5-Aminolevulinate Synthase. *Biochemistry* **37**, 1478-1484.
31. Raman, M. C. C., Johnson, K. A., Yard, B. A., Lowther, J., Carter, L. G., Naismith, J. H. & Campopiano, D. J. (2009). The External Aldimine Form of Serine Palmitoyltransferase structural, kinetic and spectroscopic analysis of the wild-type enzyme and HSAN1 mutant mimics. *J. Biol. Chem.* **284**, 17328-17339.

32. Astner, I., Schulze, J. O., van den Heuvel, J., Jahn, D., Schubert, W. D. & Heinz, D. W. (2005). Crystal structure of 5-aminolevulinate synthase, the first enzyme of heme biosynthesis, and its link to XLSA in humans. *EMBO J.* **24**, 3166-77.
33. Williams, B. B., Van Benschoten, A. H., Cimermancic, P., Donia, M. S., Zimmermann, M., Taketani, M., Ishihara, A., Kashyap, P. C., Fraser, J. S. & Fischbach, M. A. (2014). Discovery and characterization of gut microbiota decarboxylases that can produce the neurotransmitter tryptamine. *Cell Host Microbe* **16**, 495-503.
34. Vacca, R. A., Giannattasio, S., Graber, R., Sandmeier, E., Marra, E. & Christen, P. (1997). Active-site Arg --> Lys substitutions alter reaction and substrate specificity of aspartate aminotransferase. *J. Biol. Chem.* **272**, 21932-7.
35. Dajnowicz, S., Johnston, R. C., Parks, J. M., Blakeley, M. P., Keen, D. A., Weiss, K. L., Gerlits, O., Kovalevsky, A. & Mueser, T. C. (2017). Direct visualization of critical hydrogen atoms in a pyridoxal 5'-phosphate enzyme. *Nat. Commun.* **8**, 955.
36. Lin, Y. L. & Gao, J. (2011). Kinetic isotope effects of L-Dopa decarboxylase. *J. Am. Chem. Soc.* **133**, 4398-403.
37. Limbach, H. H., Chan-Huot, M., Sharif, S., Tolstoy, P. M., Shenderovich, I. G., Denisov, G. S. & Toney, M. D. (2011). Critical hydrogen bonds and protonation states of pyridoxal 5'-phosphate revealed by NMR. *Biochim. Biophys. Acta* **1814**, 1426-37.
38. Ishii, S., Hayashi, H., Okamoto, A. & Kagamiyama, H. (1998). Aromatic L-amino acid decarboxylase: conformational change in the flexible region around Arg334 is required during the transaldimination process. *Protein Sci* **7**, 1802-10.
39. Bertoldi, M., Gonsalvi, M., Contestabile, R. & Voltattorni, C. B. (2002). Mutation of tyrosine 332 to phenylalanine converts dopa decarboxylase into a decarboxylation-dependent oxidative deaminase. *J. Biol. Chem.* **277**, 36357-62.
40. Torrens-Spence, M. P., Gillaspy, G., Zhao, B., Harich, K., White, R. H. & Li, J. (2012). Biochemical evaluation of a parsley tyrosine decarboxylase results in a novel 4-hydroxyphenylacetaldehyde synthase enzyme. *Biochem. Biophys. Res. Commun.* **418**, 211-6.
41. Huang, J., Fang, H., Gai, Z. C., Mei, J. Q., Li, J. N., Hu, S., Lv, C. J., Zhao, W. R. & Mei, L. H. (2018). Lactobacillus brevis CGMCC 1306 glutamate decarboxylase: Crystal structure and functional analysis. *Biochem. Biophys. Res. Commun.* **503**, 1703-1709.
42. Liang, J., Han, Q., Ding, H. & Li, J. (2017). Biochemical identification of residues that discriminate between 3,4-dihydroxyphenylalanine decarboxylase and 3,4-dihydroxyphenylacetaldehyde synthase-mediated reactions. *Insect Biochem Mol. Biol.* **91**, 34-43.
43. Seiler, C. Y., Park, J. G., Sharma, A., Hunter, P., Surapaneni, P., Sedillo, C., Field, J., Algar, R., Price, A., Steel, J., Throop, A., Fiacco, M. & LaBaer, J. (2014). DNASU plasmid and PSI:Biology-Materials repositories: resources to accelerate biological research. *Nucleic Acids Res.* **42**, D1253-60.
44. Phan, A. P., Ngo, T. T. & Lenhoff, H. M. (1983). Tyrosine decarboxylase. Spectrophotometric assay and application in determining pyridoxal-5'-phosphate. *Appl. Biochem. Biotechnol.* **8**, 127-33.
45. Adams, P. D., Afonine, P. V., Bunkoczi, G., Chen, V. B., Echols, N., Headd, J. J., Hung, L. W., Jain, S., Kapral, G. J., Grosse Kunstleve, R. W., McCoy, A. J., Moriarty, N. W., Oeffner, R. D., Read, R. J., Richardson, D. C., Richardson, J. S., Terwilliger, T. C. & Zwart,

P. H. (2011). The Phenix software for automated determination of macromolecular structures. *Methods* **55**, 94-106.
46. Chen, V. B., Arendall, W. B., 3rd, Headd, J. J., Keedy, D. A., Immormino, R. M., Kapral, G. J., Murray, L. W., Richardson, J. S. & Richardson, D. C. (2010). MolProbity: all-atom structure validation for macromolecular crystallography. *Acta Crystallogr. D. Biol. Crystallogr.* **66**, 12-21.
47. Burkhard, P., Tai, C. H., Ristroph, C. M., Cook, P. F. & Jansonius, J. N. (1999). Ligand binding induces a large conformational change in O-acetylserine sulfhydrylase from Salmonella typhimurium. *J. Mol. Biol.* **291**, 941-53.
48. Watanabe, N., Clay, M. D., van Belkum, M. J., Cherney, M. M., Vederas, J. C. & James, M. N. (2008). Mechanism of substrate recognition and PLP-induced conformational changes in LL-diaminopimelate aminotransferase from Arabidopsis thaliana. *J. Mol. Biol.* **384**, 1314-29.
49. Wadsworth, J. M., Clarke, D. J., McMahon, S. A., Lowther, J. P., Beattie, A. E., Langridge-Smith, P. R., Broughton, H. B., Dunn, T. M., Naismith, J. H. & Campopiano, D. J. (2013). The chemical basis of serine palmitoyltransferase inhibition by myriocin. *J. Am. Chem. Soc.* **135**, 14276-85.
50. Dow, G. T., Gilbert, M., Thoden, J. B. & Holden, H. M. (2017). Structural investigation on WlaRG from Campylobacter jejuni: A sugar aminotransferase. *Protein Sci.* **26**, 586-599.
51. Winn, M. D., Ballard, C. C., Cowtan, K. D., Dodson, E. J., Emsley, P., Evans, P. R., Keegan, R. M., Krissinel, E. B., Leslie, A. G., McCoy, A., McNicholas, S. J., Murshudov, G. N., Pannu, N. S., Potterton, E. A., Powell, H. R., Read, R. J., Vagin, A. & Wilson, K. S. (2011). Overview of the CCP4 suite and current developments. *Acta Crystallogr. D Biol.* **67**, 235-42.
52. Kim, S., Chen, J., Cheng, T., Gindulyte, A., He, J., He, S., Li, Q., Shoemaker, B. A., Thiessen, P. A., Yu, B., Zaslavsky, L., Zhang, J. & Bolton, E. E. (2019). PubChem 2019 update: improved access to chemical data. *Nucleic Acids Res.* **47**, D1102-D1109.
53. Moriarty, N. W., Draizen, E. J. & Adams, P. D. (2017). An editor for the generation and customization of geometry restraints. *Acta Crystallogr. D Struct. Biol.* **73**, 123-130.
54. Chan-Huot, M., Dos, A., Zander, R., Sharif, S., Tolstoy, P. M., Compton, S., Fogle, E., Toney, M. D., Shenderovich, I., Denisov, G. S. & Limbach, H. H. (2013). NMR studies of protonation and hydrogen bond states of internal aldimines of pyridoxal 5'-phosphate acid-base in alanine racemase, aspartate aminotransferase, and poly-L-lysine. *J. Am. Chem. Soc.* **135**, 18160-75.
55. Dutta Banik, S. & Chandra, A. (2014). A hybrid QM/MM simulation study of intramolecular proton transfer in the pyridoxal 5'-phosphate in the active site of transaminase: influence of active site interaction on proton transfer. *J. Phys. Chem. B* **118**, 11077-89.
56. Robert, X. & Gouet, P. (2014). Deciphering key features in protein structures with the new ENDscript server. *Nucleic Acids Res.* **42**, W320-4.
57. Marchler-Bauer, A., Bo, Y., Han, L., He, J., Lanczycki, C. J., Lu, S., Chitsaz, F., Derbyshire, M. K., Geer, R. C., Gonzales, N. R., Gwadz, M., Hurwitz, D. I., Lu, F., Marchler, G. H., Song, J. S., Thanki, N., Wang, Z., Yamashita, R. A., Zhang, D., Zheng, C., Geer, L. Y. & Bryant, S. H. (2017). CDD/SPARCLE: functional classification of proteins via subfamily domain architectures. *Nucleic Acids Res.* **45**, D200-D203.

Supporting Information

Crystallographic snapshots of the Dunathan and quinonoid intermediates provide insights into the reaction mechanism of Group II decarboxylases

Subash Chellam Gayathri[1], Narayanan Manoj[1]*

[1] Department of Biotechnology, Bhupat and Jyoti Mehta School of Biosciences, Indian Institute of Technology Madras, Chennai-600036, INDIA

* Corresponding Author, E-mail: nmanoj@iitm.ac.in

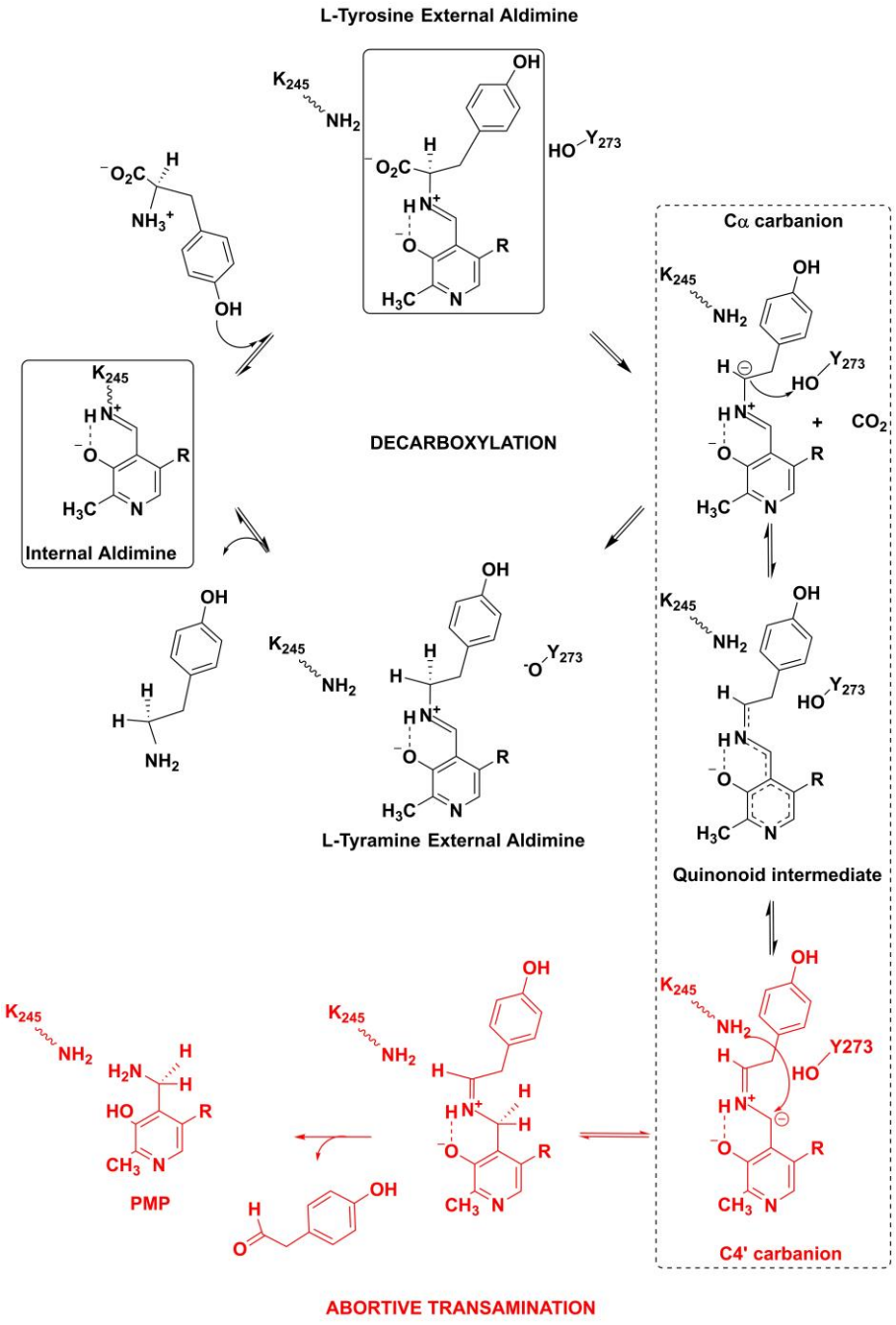

Scheme S1. Proposed mechanism of decarboxylation of L-Tyr by MjDC showing major intermediates involved in the decarboxylation reaction. Snapshots of intermediates captured *in-crystallo,* in the present study and in the previous study [18] are framed. The dash-framed intermediates are the principal resonance forms of the quinonoid intermediate that cannot be distinguished by X-ray crystallography. Reaction scheme of the complete decarboxylation reaction with replenishment of PLP is shown in black and the abortive transamination reaction with PMP production is shown in red.

Table S1. Torsion angles of ligand-aldimines in crystal structures of PLP-dependent decarboxylases

Superfamily	PDB ID	Ligand ID[a]	C4-C4'-N_{SB}-Cα (°)	C3-C4-C4'-N_{SB} (°)	C-Cα-N_{SB}-C4' (°)	Nature of complex
Group II, Fold-type I decarboxylases	**6LDS•**	0PR	-160	1	87	Substrate
	6LDT•	QND	-179	9	-	Quinonoid-like
	2OKJ[b]	PLZ (B)	-121	-54	108	Mixed-substrate
	1JS3	142 (A)	88	-71	171	Inhibitor
		142 (B)	0.01	-63	168	Inhibitor
	4E1O[b]	PVH (A)	165	-149	-99	inhibitor
		PVH (B)	155	-130	-113	inhibitor
		PVH (C)	164	-144	-104	inhibitor
		PVH (D)	160	-142	-101	inhibitor
		PVH (E)	151	-141	-104	inhibitor
	4OBV[b]	3SO (A)	180	-37	-174	inhibitor
		3SO (B)	-179	-47	-150	inhibitor
		3SO (D)	-179.	-29	145	inhibitor
	6EEM	0PR (A)	179	-120	141	Substrate[$]
All other Fold-type I decarboxylases	**1LC8**	33P (A)	179	-25	-	Intermediate
	1WYV	AOA (B)	-179	-60	-	inhibitor
		AOA (D)	-178	-53	-	inhibitor
		AOA (F)	-179	-73	-	inhibitor
	1D7R	5PA (A)	166	-78	-98	inhibitor
	1D7S	DCS (A)	-128	12	-	inhibitor
	1D7U	LCS (A)	-157	-9	-	inhibitor
	1D7V	NMA (A)	-153	50	132	inhibitor
	1M0N	HCP (A)	-163	3	-161	inhibitor
	1M0O	MPM (A)	-179	-6	-140	inhibitor
	1M0P	ELP (A)	164	-63	-79	inhibitor
	1M0Q	EPC (A)	-169	0.1	-160	inhibitor
Fold-type III decarboxylases	**1KO0**	LYS (A)	161	45	130	Substrate
	2QGH	LYS (A)	-172	-46	38	Substrate
	1NJJ	ORX (A)	163	-36	-65	Substrate analog
		ORX (A)	152	22	-89	Substrate analog
		ORX (A)	146	-0.3	-87	Substrate analog
		ORX (A)	154	65	168	Substrate analog
	1F3T	PUT (A)	-179	-32	-	Product
		PUT (B)	-175	-2	-	Product
		PUT (C)	180	-48	-	Product
		PUT (D)	-170	21	-	Product
	2NVA	PL2 (A)	-145	28	-	Product
		PL2 (B)	-136	24	-	Product
		PL2 (C)	-144	23	-	Product
		PL2 (D)	-140	27	-	Product
		PL2 (E)	-142	26	-	Product
		PL2 (F)	-144	23	-	Product
		PL2 (G)	-146	26	-	Product
		PL2 (H)	-145	19	-	Product
	2TOD	DMO (A)	173	-54	-4	inhibitor
		DMO (B)	170	-58	12	inhibitor
		DMO (C)	168	-55	3	inhibitor
		DMO (D)	-175	-53	-6	inhibitor
	3C5Q	LYS (A)	-171	-45	-	Substrate*

*External aldimine formed with the ε-amine of Lys substrate.

[a] Chain ID is shown within brackets ()

[b] The catalytic loop in an ordered and closed conformation identical to that in apoMjDC•PLP_{ALD}

$ Unpublished

• This study

Table S2: Pairwise RMSD (Å) between the structures.

	holoMjDC•LLP	Apo-K245A	PLP-K245A	PLY-K245A	QND-K245A	R371A
K245A	0.13 (382)					
PLP-K245A	0.15 (382)	0.09 (381)				
PLY-K245A	0.14 (383)	0.09 (381)	0.12 (382)			
QND-K245A	0.3 (385)	0.16 (382)	0.09 (382)	0.11 (382)		
R371A	0.19 (389)	0.21 (381)	0.24 (381)	0.24 (382)	0.38 (384)	
apoMjDC•PLP_{ALD}	0.34 (384)	0.31 (381)	0.36 (381)	0.35 (381)	0.46 (384)	0.34 (383)

Value in parentheses refers to the number of aligned Cα atoms between each pair.

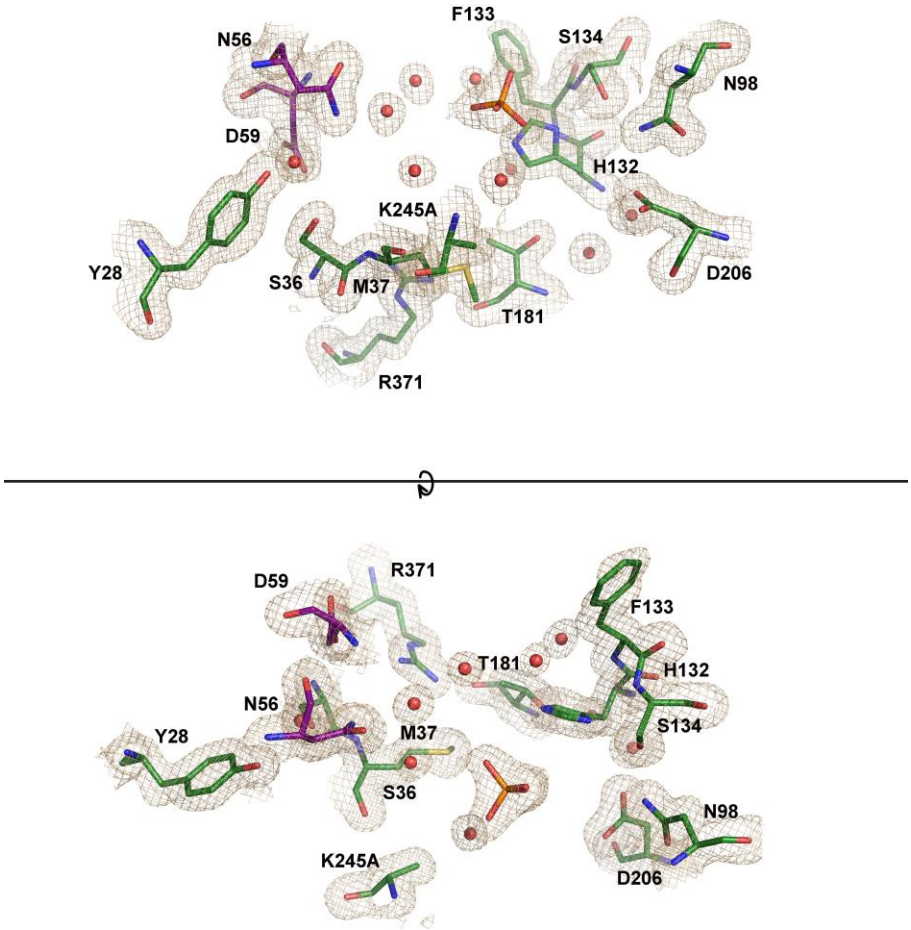

Figure S1. Close up view of active site of apo-K245A. (A) Two views of the active site of K245A rotated (ca. 90°) along the x axis are shown. 2Fo−mFc map (contoured at 0.8 σ) of active site residues is shown as brown mesh representation. Residues are shown as green and purple (adjacent subunit) sticks. Phosphate is shown as orange sticks.

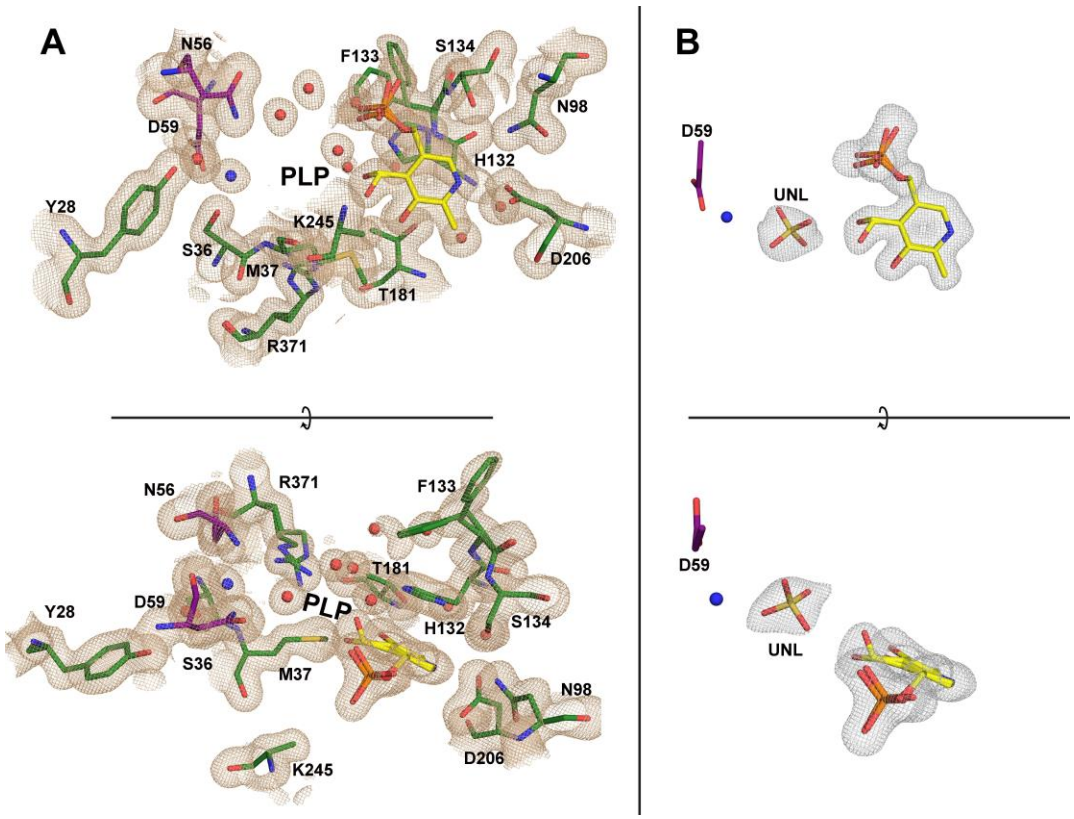

Figure S2. Close up view of active site of PLP-K245A. (A) Two views of the active site of PLP-K245A rotated (ca. 90°) along the x axis are shown. 2Fo−mFc map (contoured at 0.8 σ) of active site residues is shown as brown mesh representation. Residues are shown as green and purple (adjacent subunit) sticks, PLP is shown as yellow sticks, and waters are shown as red spheres. Ammonium ion is shown as blue sphere (B) mFo−DFc omit map (contoured at 3.0 σ) corresponding to a simulated annealing omit map (5000 K) calculated from a model lacking the atoms of PLP and the unknown ligand is shown as grey mesh. PLP and the unknown ligand (modelled as sulphate for the sake of figure reference) were superposed on the map and is shown as yellow sticks.

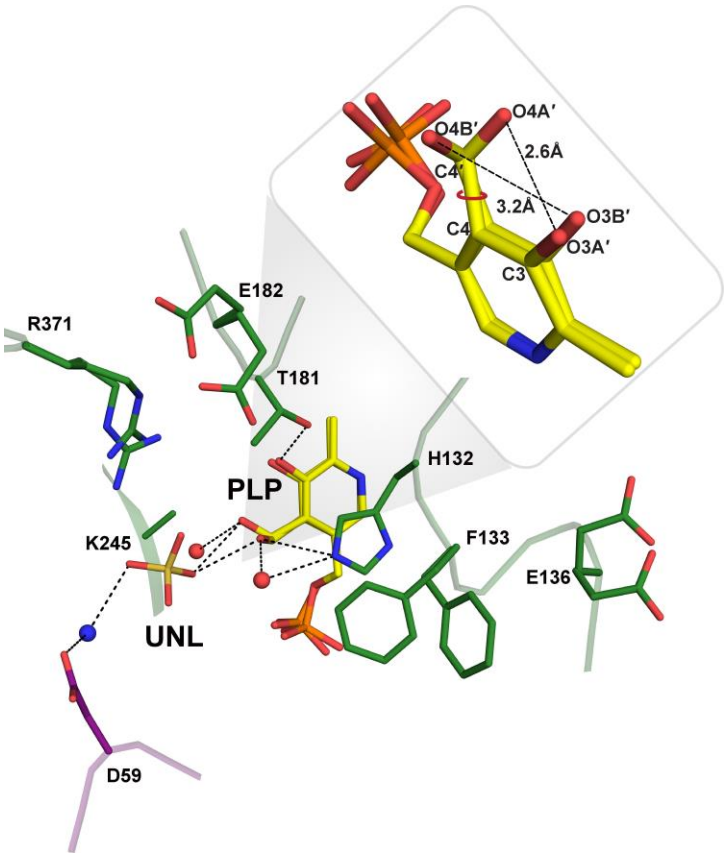

Figure S3. Geometry of interactions of pyridoxal-P in the active site of PLP-K245A. View of the active site of PLP-K245A. Residues from subunit A and B are shown as green and purple sticks, respectively. Pyridoxal-P was modelled in two conformations and is shown in yellow. Waters are shown as red spheres and ammonium ion shown as blue sphere. Hydrogen bond interactions (<3.2 Å) are displayed as dashed black lines**.** Inset shows a magnified view of the two conformers of pyridoxal-P showing two different torsion angles measured along O4A′-C4′-C4-C3 (-62°) and O4B′-C4′-C4-C3 (1.7°).

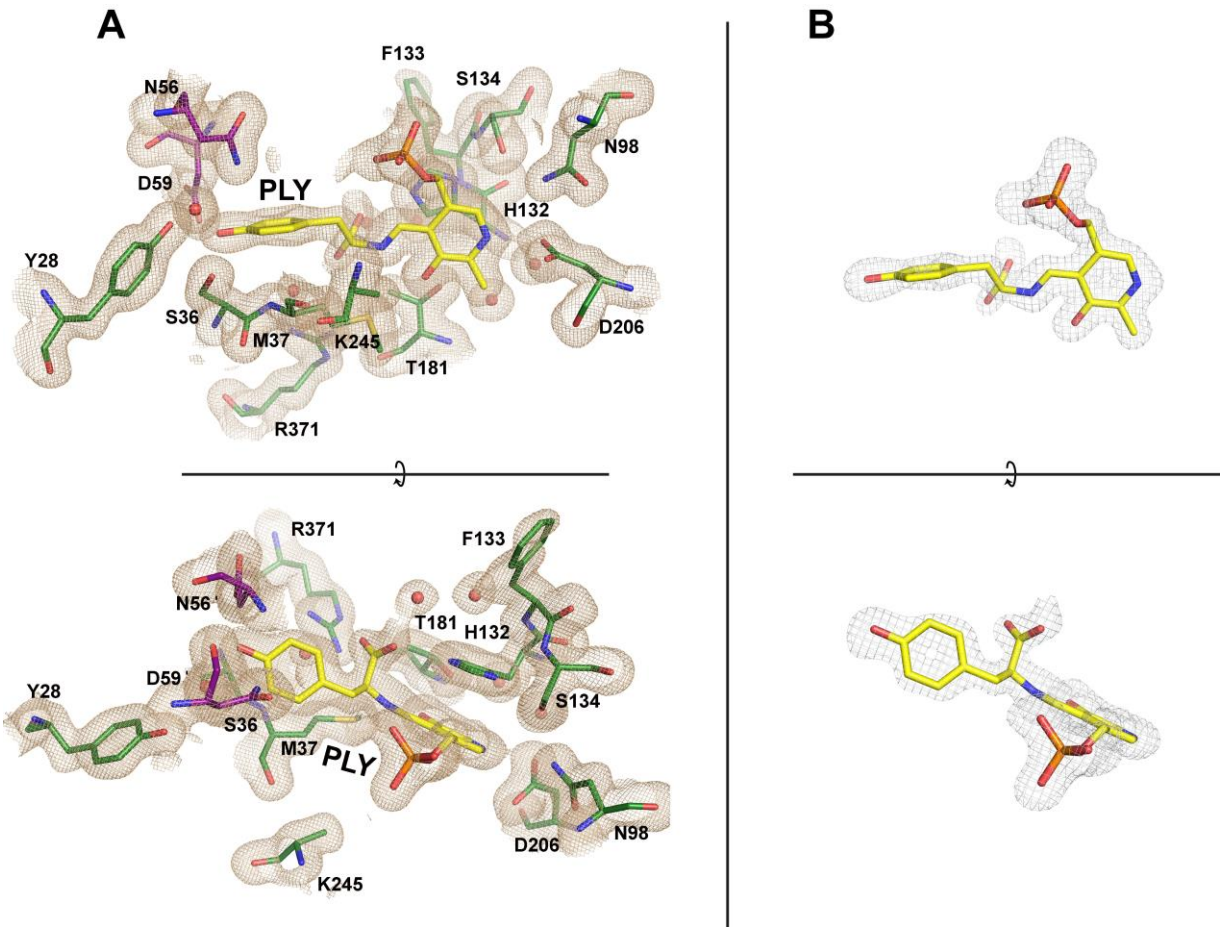

Figure S4. Close up view of PLY in the active site of PLY-K245A. Two views of the active site of PLY-K245A rotated (ca. 90°) along the x axis are shown. (A) 2Fo−mFc map (contoured at 0.8 σ) of active site residues is shown as brown mesh. Residues are shown as sticks in green and purple (adjacent subunit), PLY is shown as yellow sticks, and waters are shown as red spheres. (B) mFo−DFc omit map (contoured at 3.0 σ) around PLY is shown as grey mesh and corresponds to a simulated annealing omit map (5000 K) calculated from a model lacking the atoms of PLY. Modeled PLY is shown as yellow sticks.

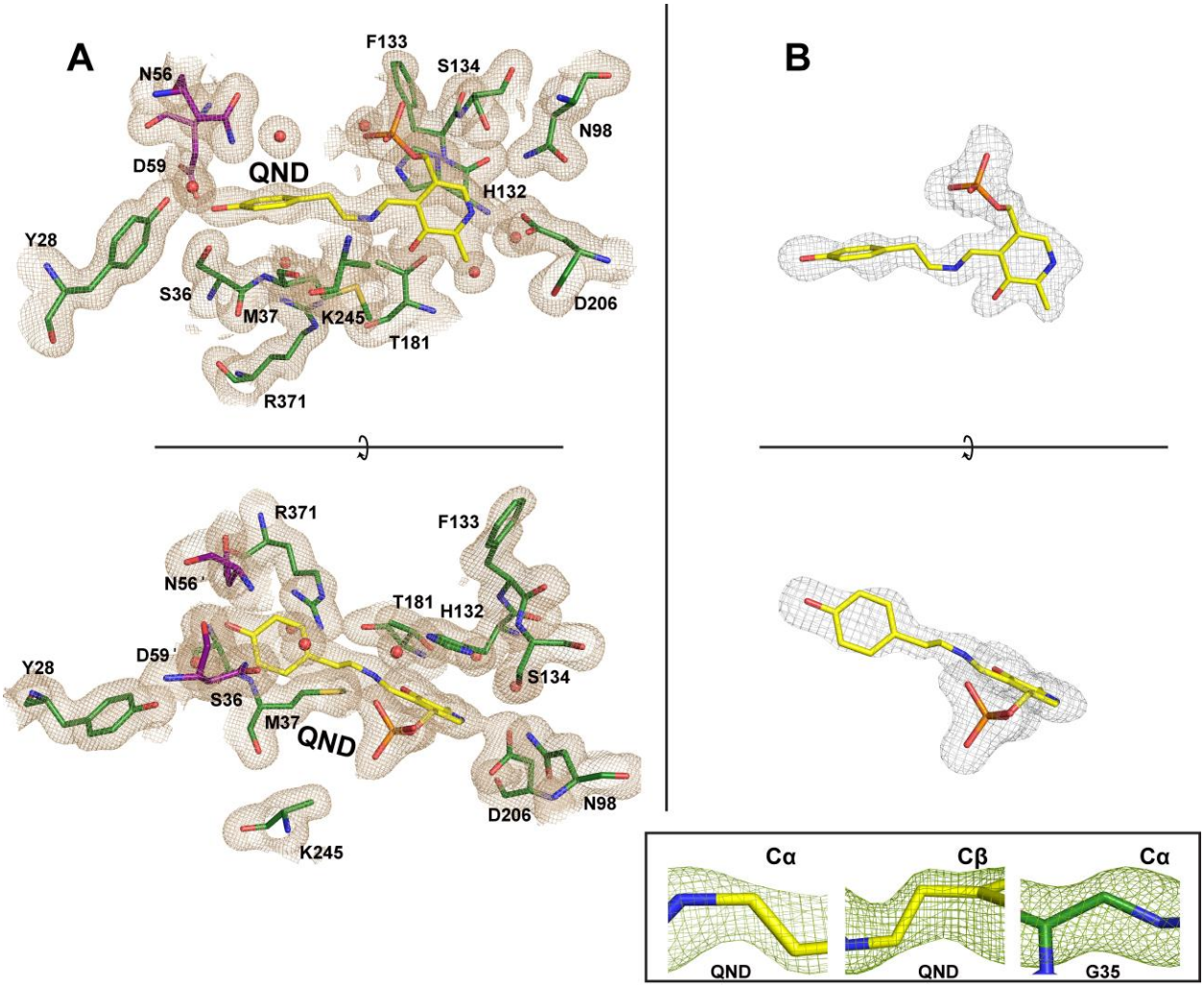

Figure S5. Close up view of QND in the active site of QND-K245A. Two views of the active site of QND-K245A rotated (ca. 90°) along the x axis are shown. (A) 2Fo−mFc map (contoured at 1.0 σ) of active site residues is shown as brown mesh. Residues are shown as green and purple (adjacent subunit) sticks, QND is shown as yellow sticks, and waters are shown as red spheres. (B) mFo−DFc omit map (contoured at 3.0 σ) around QND is shown as grey mesh and corresponds to a simulated annealing omit map (5000 K) calculated from a model lacking the atoms of QND. QND was superposed on the map and is shown as yellow sticks. Inset shows mFo−DFc omit maps around Cα-QND, Cβ-QND and the Cα of an adjacent Gly35 residue for comparison. Densities of Cβ-QND and Cα-Gly35 correspond to that of a sp^3 hybridized tetrahedral geometry while the Cα-QND displays a trigonal planar geometry indicating sp^2 like hybridization.

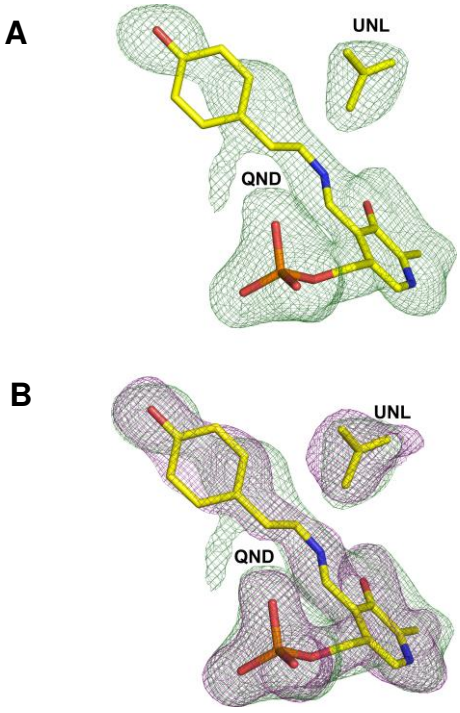

Figure S6. Electron density maps of the QND ligand obtained from different data sets. Panel A shows the omit map of QND (green) from a crystal soaked for 24 hrs with the substrate and panel B shows a superposition of the omit maps of QND obtained from the two different data sets. The purple mesh represents the best dataset for the QND ligand. The maps are contoured at 3σ and represented in mesh format. The QND and UNL ligands are shown as stick representation (yellow).

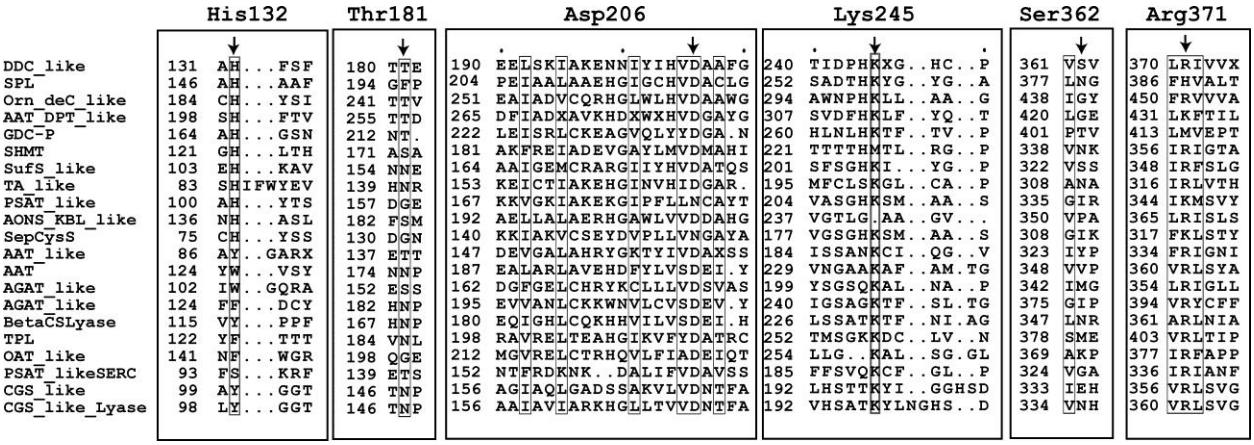

Figure S7. Representative blocks taken from a structure based sequence alignment of proteins belonging to the different subfamilies of the fold-type I superfamily. The blocks show very high conservation at the postion of the active site Lys245, Asp206 and Arg371 (indicated by arrows). Other residues discussed in the study are also indicated by arrows. The representative set of sequences were taken from NCBI's Conserved Domain Database [36].

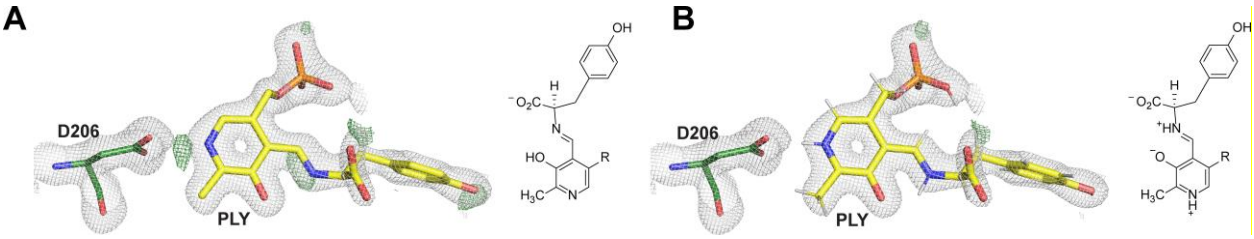

Figure S8. Resultant electron density maps of PLY after crystallographic refinement of two different protonation states of PLY in PLY-K245A (A) unprotonated N1 and N_{SB} atoms (B) protonated N1 and N_{SB} atoms (see Experimental Procedures). The respective schemes are shown for reference. The 2Fo−mFc map (grey mesh, contoured at 1.5 σ) and the mFo−DFc difference map (green mesh, contoured at 3.6 σ) are shown. Refinement with unprotonated states resulted in residual densities around N1 and N_{SB} atoms in the difference Fourier maps whereas the residual densities were absent when refined with protonated states. The conserved Asp206 that forms a H-bond with the protonated N1 is shown as green sticks.

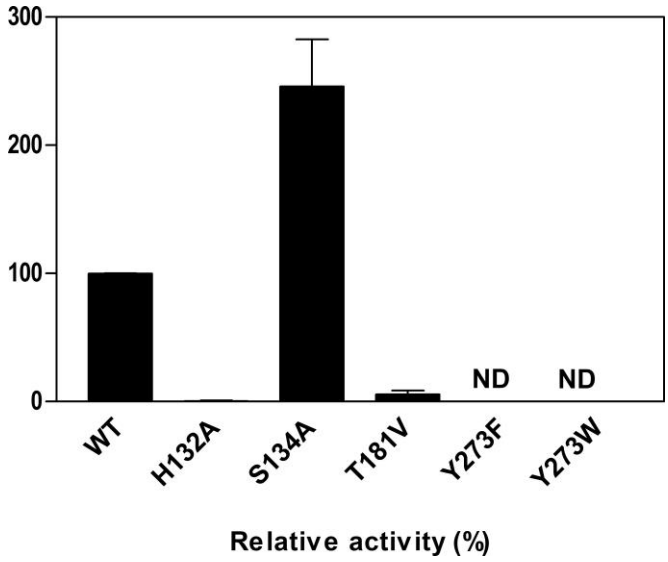

Figure S9. Relative activity of MjDC WT and mutants of the extended hydrogen bonding network. The specific activity of the WT enzyme towards L-tyrosine is set to 100 %. The error bar represents the standard deviation between triplicates. For the Tyr273 mutants (Y273F and Y273W) no detectable activity was observed at standard assay conditions, denoted as ND. The figure is adapted from our previous study on the mutants [1].

Table. S3. List of oligonucleotides used for mutagenesis

Mutant	Oligonucleotide sequence
K245A	*5′-GATTGGGCAGTGCCCCATTGCATGGGGGTCTATGGTTATA-3′*
	5′-TATAACCATAGACCCCCATGCAATGGGGCACTGCCCAATC-3′
R371A	*5′-TGTGGCATAACAACGATTGCCAAAGCTTTAACACAATTGC-3″*
	5′-GCAATTGTGTTAAAGCTTTGGCAATCGTTGTTATGCCACA-3′
H132Q	*5′-ATCGTTCCAATAACTGCCCAGTTCTCATTCGAAAAAGGAAG-3′*
	5′-CTTCCTTTTTCGAATGAGAACTGGGCAGTTATTGGAACGAT-3′
D59A	*5′-CCCTTTAAATAGTCCAGGGGCTCCCAAGTTTGTTTCTAA-3′*
	5′-TTAGAAACAAACTTGGGAGCCCCTGGACTATTTAAAGGG-3′

References:

[1]. Chellam Gayathri, S. & Manoj, N. (2019). Structural insights into the mechanism of internal aldimine formation and catalytic loop dynamics in an archaeal Group II decarboxylase. *J. Struct. Biol*. **208**, 137-51.